OXIDE-COATED VERTICALLY ALIGNED CARBON NANOTUBE FORESTS AS THERMAL INTERFACE MATERIALS

A Thesis

Presented to

The Academic Faculty

By

Cristal Jeanette Vasquez

In Partial Fulfillment

Of the Requirements for the Degree

Master of Science in the

School of Mechanical Engineering

Georgia Institute of Technology

August 2014

OXIDE-COATED VERTICALLY ALIGNED CARBON NANOTUBE FORESTS AS THERMAL INTERFACE MATERIALS

Approved by

Dr. Baratunde Cola, Advisor
School of Mechanical Engineering
Georgia Institute of Technology

Dr. Samuel Graham
School of Mechanical Engineering
Georgia Institute of Technology

Dr. Kyriaki Kalaitzidou
School of Mechanical Engineering
Georgia Institute of Technology

Date Approved: 4/16/14

ACKNOWLEDGEMENTS

This work would not have been possible without the support of many people. I would first like to thank my advisor Dr. Baratunde Cola, for his support and guidance. I would also like to thank Dr. Samuel Graham and Dr. Kyriaki Kalaitzidou for serving on my committee. I am grateful to have had such a supportive and selfless collaborator in Virendra Singh. I would also like to thank Tom Bougher and John Taphouse for sharing their expertise and always taking time out of their schedule to help me throughout this work. Lastly, I would like to thank Matthew Smith, Pablo Salazar, and the entire NEST group for the interesting conversations, laughs, and shared times.

I would like to acknowledge the Georgia Tech Institute for Electronics and Nanotechnology (IEN), especially Charlie Suh, Ben Holerbach, Chris Yang and John Pham for their timely responses and continued support to keep equipment operative. Research for this work was supported by Universal Technology Corporation, Dayton, OH.

TABLE OF CONTENTS

LIST OF TABLES

LIST OF FIGURES

SUMMARY

Carbon nanotube (CNT) forests have outstanding thermal and electrical properties, which have generated significant interest as thermal interface materials (TIMs). Some drawbacks to using CNTs as TIMs include poor substrate adhesion, high interface resistances inhibiting thermal transport, and lack of electrical insulation in particular electronic component applications. It is thus useful to be able to modify CNTs to reduce their electrical conductivity while maintaining high thermal conductivity and interface conductance, and high mechanical compliance. A recent report suggests that nanoscale oxide coatings could be applied to CNTs in forests without changing the mechanical deformation behavior of the forests. Oxide coatings could also provide temperature and environmental stability as well as better adhesion to the substrate compared to pristine CNT forests. A major commercial motivation for this work is that thermal management materials for LEDs and power electronics are on the rise. This falls in correlation with Haitz's Law, which states that every decade, the cost per lumen falls by a factor of 10, and the amount of light generated per LED package increases by a factor of 20. Sensitivity to weight and cost forces these two markets to rely on special TIMs, rather than secondary heat sinks.

In this study, we investigated the thermal and electrical resistance of CNT forests with an oxide coating, and we characterized their chemical composition. Low-pressure chemical vapor deposition (LPCVD) was used to produce CNTs on high-conductivity Si substrates. Plasma-enhanced atomic layer deposition (PALD) was used to deposit Al_2O_3 on individual CNTs in forests. This process was facilitated by O_2 plasma pretreatment to functionalize the surfaces of the CNTs and to nucleate the oxide growth. Other material coatings, including AlN, Pt, and ZnO were also deposited on CNTs with PALD to compare and possibly enable tunable functions with this approach. Several analytical techniques were used to characterize the CNT-oxide composites, including scanning electron microscopy, Raman spectroscopy, and X-ray

photoelectron spectroscopy. Thermal conductivity and thermal interface resistance were measured for pristine and conformal oxide-coated CNT forests using a modified photoacoustic technique. The oxide coating had no significant effect on the effective thermal conductivity of the forests, in contrast to expectations of increased phonon scattering in the CNTs as a result of the oxide boundary. Thermal interface resistance increased modestly for oxide coatings thicker than 3 nm; this was expected due to increased stiffness and decreased contact area at the interface. Electrical resistance measurements were made, and a fivefold increase was observed for the oxide-coated forests at 0.5 nm, 1 nm and 3 nm. The best combination of low thermal resistance and high electrical resistance was the 0.5 nm coating with a total thermal resistance value of ~11 mm^2K/W, and a total electrical resistance value of ~40 Ω. But the 0.5 nm coating was not conformal and the 3 nm thick coating was, it produced a total thermal resistance value of ~25 mm^2K/W, and a total electrical resistance value of ~50 Ω. Thus the optimal coating thickness falls between 0.5 nm and 3 nm. This approach could emerge as a promising route to create a viable TIM for thermally conductive and electrically insulating applications.

1. INTRODUCTION

1.1 Motivation and Application

As electronics become smaller in size, lighter in weight, and are further packed with enhanced performance capabilities, power density continues to rise and thermal management becomes more problematic. Industry does not want to increase product size as a result of additional processing capability, and its reluctance drives conflicting needs.[1] We already see this today with products such as the iPad, which reaches temperatures of 116 °F – this is warm enough to limit the amount of time that consumers can hold iPads on their laps without suffering burns.[2] Heat generated by these electronics must be dissipated in order to improve reliability and prevent premature failure. Heat can be removed in many different ways, which include: venting, enclosure fans, thermal interfaces, passive heat sinks, active heat sinks, and heat pipes.[1] The chosen solution would likely depend on system parameters, which would vary if the system is being designed for performance or reliability, and cost or manufacturability of the chosen scheme. The best design is always the preventive design that addresses thermal issues early in the design process to reduce cost and minimize rework.

It is important to realize that a major bottleneck in thermal management is the interface between the heat source and the heat sink. A thermal bottleneck is defined as a location where there is substantial heat flow in a restricted area. Bornoff et al completed a simulation that shows the largest bottlenecks are not at the heat sources or heat sinks themselves but at the contact surfaces.[3] This is where thermal interface materials come into play; they can effectively increase the contact area at these interface surfaces by filling microscopic air gaps caused by variations in surface roughness even among the smoothest surface finishes[1] (as shown in Figure 1.1). They can also help to spread heat without changing the geometry or material because they

have higher thermal transport properties in the direction of heat being dissipated.[4] This effectively reduces cost and large implementation turnaround times.

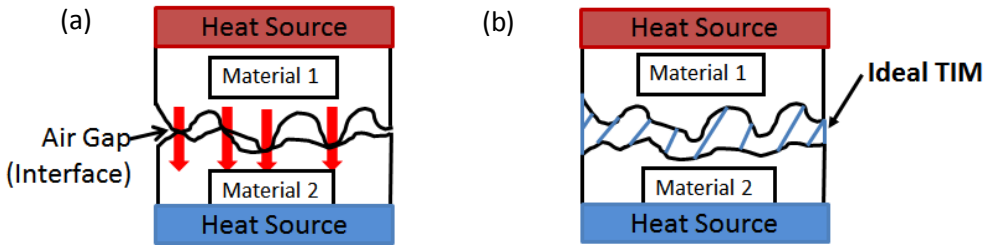

Figure 1.1 Schematic of (a) real interface vs. (b) ideal thermal interface material, with very high thermal conductivity and almost no material resistance

From a market perspective, thermal management material for light-emitting diodes (LEDs) and power electronics is projected to be a $4.8 billion market by 2020; this is more than double the $1.8 billion market in 2013.[5] LEDs specifically require vary low operating temperatures, due to the result in color shift with temperature rise, and they currently use TIMs for thermal management.[6] Thus manufacturers will be seeking more cost effective ways to improve heat dissipation while not sacrificing size or weight. These markets will rely on special TIMs rather than large bulky secondary heat sinks. The demand for TIMs will also rise in the smart phone and tablet industry, with a projected $300 million thermal material market in 2020.[5] This is falls in parallel with Hait's law, which states that every decade the cost per lumen falls by a factor of 10; and the amount of light generated per LED package increases by a factor of 20 for a given wavelength of light. [7]

Three specific applications where TIMs are currently used and an electrically insulating TIM is applicable are: insulated-gate bipolar transistor (IGBTs), and light-emitting diode (LED) applications. Figure 1.2[8] is a schematic of an LED package where there is a conductive dielectric layer labeled above the bottom aluminum base, and below the aluminum base would be an electrically isolating and thermally conductive material adhered to a heat sink. An electrically insulating TIM is used in the conductive dielectic layer and the electrically isolating and thermally conductive layer. The Bergquist company have these electrically isolating and

thermally conductive materials that have thermal resistances > 280 mm^2K/W with volume resistivity of 10^{11} Ω*m.[8] Figure 1.3[9] is a schematic of an IGBT module assembly, where is being dissipated from the IGBT down to the AlSiC baseplate labeled on the assembly. The AlN substrate serves as the thermally conductive and electrically insulating material which could be replaced with an electrically insulating TIM. AlN, BeO and SiC are all thermally conductive ceramic substrates whose thermal conductivities range from 70 - 300 W/mk and have a volume resistivity of 10^{12} Ω*m.[10]

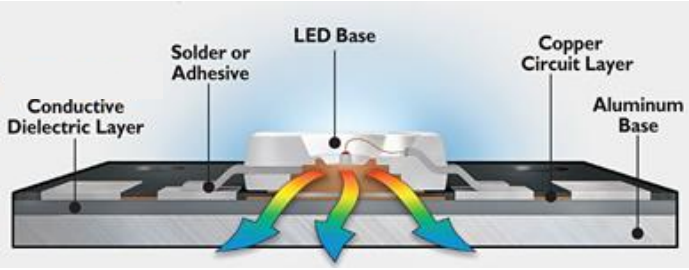

Figure 1.2 Schematic of light-emitting diode (LED) package with labeled conductive dielectric layer and aluminum base on the bottom

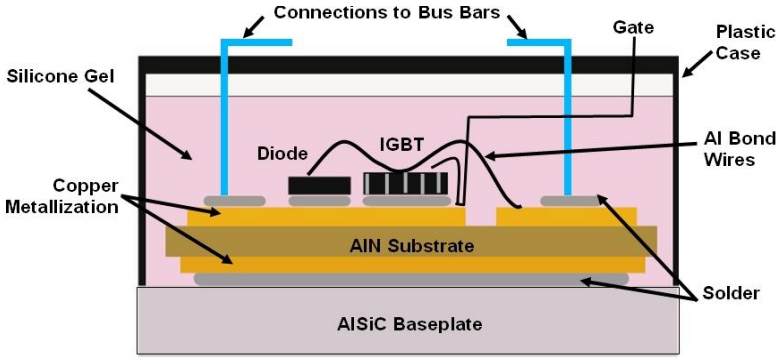

Figure 1.3 Schematic of an insulated-gate bipolar transistor (IGBT) module assembly with heat being dissipated from the IGBT down to the AlSiC baseplate

Thus TIMs need to have the following characteristics to be successful on the market:

- Low coefficient of thermal expansion (CTE) to reduce mismatch problems between bonded interfaces, which lead to large stresses on the device and TIM especially with solder. [11]

- Thermal resistances < 5 mm^2K/W for high power density applications, currently restricted by thickness or thermal conductivity[12, 13]

- Electrically insulating thermal interface materials[13] with higher thermal resistances (current electrically insulating TIMs thermal resistances > 20 mm^2K/W)

- Mechanical compliance ('soft'), to conform to surface roughness of interface.[6]

- No pump out or dry out over time, as with thermal greases and gels.[12]

- Thermal fatigue, primarily in metal thermal interface materials[13]

The toughest characteristics to meet are mechanical compliance and low thermal resistances because materials with very high thermal conductivities are typically hard bulk materials which are not compliant. Because a TIM constitutes a significant fraction of the total thermal resistance from a heat source to a heat sink, and because all electronic systems are looking to reduce mass and increase performance, programs such as the Defense Advanced Research Projects Agency (DARPA) are focused on developing nano-thermal interfaces.[14] Nano-materials are being studied as viable alternatives to bulk materials, as they allow for further exploitation of material properties such as: aspect ratios, nanoscale material properties, and surface interactions. Manipulation of these properties may render nano thermal interfaces which allow systems to operate at higher power densities for longer periods of time while also reducing size and weight.[14]

Thus oxide coated VACNT forests could be a nano thermal interface solution for these thermally conductive and electrically insulating applications because they have promising

material properties. Carbon nanotubes large aspect ratios make them mechanically compliant effectively reducing contact resistance and coefficient of thermal expansion problems. There is no chance of pump out or dry out and the oxide coating would provide electrical insulation. The oxide coated VACNT forests are also much thinner with comparable to better thermal conductivity values than the current Bergquist Company pads or AlN solutions providing lower layer resistances.

Oxide coatings are important not only for electrically insulating materials for TIM applications but also for materials in microelectronics. They can be used in high k dielectric materials, where they may serve as replacements for the silicon channel material in complementary metal-oxide semiconductor (CMOS) technologies with single-wall carbon nanotubes (SWCNTs).[15, 16] If this is accomplished, it may allow for smaller metallic CNT-based interconnects to be used in transistors of reduced size, since the compatibility of the CNT growth process within the current CMOS may no longer be an issue. [17] Oxide coated CNTs could also be used in field effect transistor (FET) materials, thin film transistors (TFT) for organic light-emitting diodes (OLED), and supercapacitors.[18] Another application outside the electronics and semiconductor industry is H_2 generation by metal-oxide based solar thermal water splitting, where CNTs would serve as the metal, as they have much higher thermal conductivity values than other typical metals.[19] If we look at this in reverse, and the electrical conductivity of the oxide or Al_2O_3 specifically is increased by the vertically aligned multiwall carbon nanotubes (MWCNTs), then this type of composite is useful for: heating elements, electrical igniters, electromagnetic and antistatic shielding of electronic components, electrodes for fuel cells, and crucibles for vacuum induction furnaces.[20]

Consequently an electrically insulating and thermally conductive material could have a large impact in the microelectronics industry and it is important for us to understand the thermal transport of an oxide coated VACNT forest, as well understand the electrical insulation that an oxide coating may provide a VACNT forest. This research seeks to address these thermal and

electrical transport issues by performing thermal and electrical transport measurements as well as a chemical characterization analysis to support the evidence.

1.2 Objective and Research Approach

The objective of this work is to develop a thermally conductive and electrically insulating vertically aligned carbon-nanotube-based material with uniformly thick oxide coatings and to answer several fundamental questions related to the processing of oxide-coated CNTs for use in a variety of other applications. Vertically aligned carbon nanotubes are used because they can solve some of the most difficult TIM problems, which are discussed in Chapter 2.1. The research approach implemented was motivated by the following questions:

- Can CNTs be functionalized by oxygen plasma without damaging their quality?
- What is the thinnest oxide coating we can achieve that is conformal and uniform from the CNT tips to roots?
- What is the maximum forest height that could be coated uniformly?
- Is the coating crystalline or amorphous? How does this degree of crystallinity and thickness of the coatings affect the thermal conductivity of the VACNT layer?
- What is the thickest conformal oxide coating that could be applied to vertically aligned carbon nanotubes (VACNTs) without altering their mechanical compliance significantly?
- What is the thermal resistance of the oxide coated VACNT forest layer? How do the various oxide coating thicknesses compare to the bare VACNT forests? What is the total thermal resistance and does stiffness play a major role in interface resistance?
- What is the electrical resistance of the oxide coated VACNT layer? How do the various oxide coating thicknesses compare to the bare VACNT forests? What is the total electrical resistance and does stiffness play a major role in interface resistance?
- Are the oxide coated VACNT chemically stable in air? Are they more stable than

VACNT alone? Up to which temperatures are they stable?

These questions are tested and answered throughout the work of this thesis. This approach was used as a means to develop a controlled process to fabricate and characterize the chemical composition of uniformly thick conformal oxide coated VACNT forests (as described in Chapter 4). The approach also served to test and document their electrical and thermal transport properties (as described in Chapter 5).

2. BACKGROUND

2.1 Vertical Carbon Nanotube Forest Characteristics

Carbon nanotubes are a unique material in nature due to their large aspect ratios and efficient thermal and electrical transport properties. This makes them a great candidate for a thermal interface materials which require mechanical compliance and efficient thermal transport across the interface. The CNT structure is composed of a rolled up hexagonal graphene structure that may be grown as a single-wall CNT or as a multiwall CNT ("Russian doll" structure), typically with capped ends.[21] Multiwall CNTs have measured thermal conductivity values as high as 3000 W/mK[17] and electrical resistance on the order of 10^5 Ω.[16] Individual multiwall CNTs have also reported measured young's modulus of 1000 GPa, which enables them to withstand large stresses with little elastic deformation.[18] Atomic force microscopy measurements on an individual vertically aligned multiwall CNT show that the tube is extremely flexible under large strains and are resistant to failure under repeated bending in the axial direction, where reversible periodic buckling of nanotubes was observed; proving that MWCNTs have great mechanical compliance due to their large aspect ratios.[22] Lastly CNTs are chemically robust and chemically stable in air up to ~450°C.[23]

Although individual CNTs have efficient transport properties, they have not been exploited when grown in forest or sheet form. In this work we use vertically aligned carbon nanotube (VACNT) forests (seen in figure 2.1), because the axial alignment provides improved thermal conductivity over CNTs grown in random orientations and their large aspect ratios in an array provide a 'soft' or compliant structure. CNTs also have strong inter-tube van der Waals interactions, which help them stay aligned in a forest.[24] The effective moduli in compression for vertically aligned CNTs has been measured to be 0.03-0.3 GPa, orders of magnitude lower than individual CNTs which makes them less stiff and more compliant.[25] VACNT forests do buckle and experience vertical shear offsets when loaded by a flat punch indenter with ~ 1 MPa stress,

therefore this is their maximum allowable stress before buckling.[26] Thermal conductivities of VACNT forests have been reported to fall between 0.5 - 267 W/mK.[27] Conductivity across the VACNT forest is hindered by the packing density, by damage or defects as a result of fabrication technique, and by boundary resistance between the forest and the substrate or other contact material.[17, 28] Although the thermal conductivity of a VACNT forest is comparable to that of current TIMs, it still has favorable characteristics which include better mechanical compliance, thinner TIMs (CNT heights grown by CVD range from 1s – 100s of μm[29]) compared to current pads on the market (which are mm thick)[8] for reduced resistance, no possibility of dry out, and reduced coefficient of thermal expansion mismatch problems.

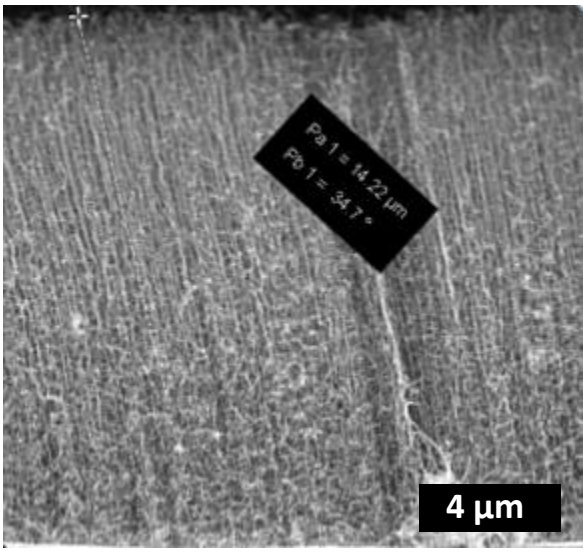

Figure 2.1 Side view of vertically aligned carbon nanotubes grown by low pressure chemical vapor deposition, the inset text shows the height of the forest at ~ 14 µm

2.2 Oxide-Coated Vertically Aligned Carbon Nanotube Forests

If we could conformally-coat CNTs, we could potentially create an electrically insulating and a highly thermally conductive material. Much research has focused on deposition of uniform thin films onto CNTs; that has yielded various coating techniques that can be divided into three basic categories; electrodeposition, physical vapor deposition (PVD), and chemical vapor

deposition (CVD). These different deposition techniques have been shown to affect crystallinity, morphology, and deposition precision in prior work.[28, 30, 31]

Electrodeposition tends to be the quickest, most scalable, and cheapest method for coating CNTs, but its major drawback is control of the deposition as seen in prior work.[28] Layer deposition depends on the current density and time of flow, but naturally the metals form agglomerates. Consequently an optimized pulsing technique must be used to stop particle growth and maintain small particle sizes.[28] Another problem with electrodeposition is that it requires the VACNT forests to be immersed and these structures are delicate whose alignment would not be preserved.[30] Physical vapor deposition (PVD), is accomplished by a metal by using heating or ion bombardment to evaporate a metal, which then condenses onto a cold substrate.[28] PVD systems often times overshoot by a few nanometers and deposit large particle sizes depending on the deposition rate; consequently sometimes only the top layer of a forest is metallized or the metal deposited has large void spaces.[32] PVD has been used to coat individual CNTs in forests with tungsten, but deposits a layer of particles along the CNT sidewalls instead of conformal coatings as shown in figure 2.2. [33]

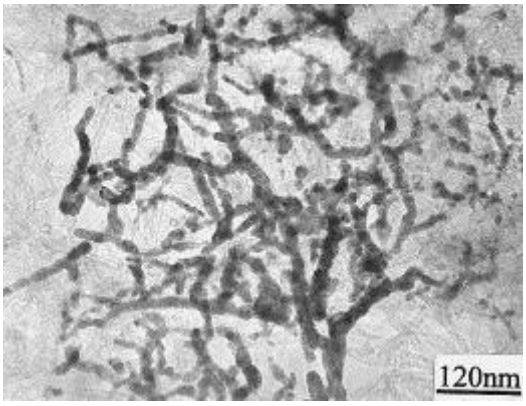

Figure 2.2 Individual CNTs in forests coated with tungsten by physical vapor deposition

Chemical vapor deposition (CVD), is accomplished by bringing a reactant gas mixture into contact with the surface to be coated, where it decomposes and deposits a dense pure layer of material of nano thickness.[28] Chemical vapor deposition has also been used to coat various metals on suspended single-wall carbon nanotubes (as seen in Figure 2.3), continuous and quasi-

continuous coatings were achieved but they were not conformal, the growth was made up of spherical particles.[34] A metal-organic chemical vapor deposition of thermally decomposed iron pentacarbonyl $Fe(CO)_5$ (as seen in Figure 2.4), has been used to achieve conformal coatings throughout a VACNT forest but the drawback is the high deposition rate of 2-3nm/cycle which does not allow for precise control of the coating thickness.[30] Atomic layer deposition (ALD) is similar to CVD except it breaks the reaction into two half reactions; this allows for controlled film growth as fine as 0.01nm per cycle.[31] Consequently it is the most controllable coating process, although it is not as fast or as economical as electrodeposition.

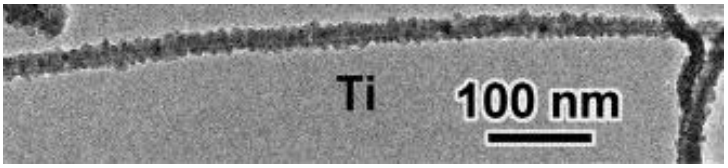

Figure 2.3 Single-wall CNT coated with titanium by chemical vapor deposition

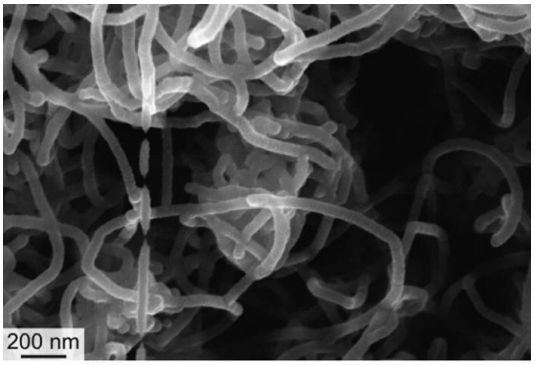

Figure 2.4 Metal-organic chemical vapor deposition of thermally decomposed iron pentacarbonyl $Fe(CO)_5$ on vertically aligned CNT forest

Atomic layer deposition has been used to achieve conformal and uniform thick coatings of transition-metal oxides[35] and Al_2O_3[36, 37] on dispersed CNTs on both the outer and inner walls. ALD has also been used to coat single-wall CNTs with Al_2O_3 but the growth was in spherical deposits and a conformal coating was not achieved.[15] When Abadi et al. used ALD to deposit Al_2O_3 coatings on VACNT forests, adjusting exposure times allowed for conformal Al_2O_3 coatings within the forest. [38] These Al_2O_3 coatings were now conformal but not uniformly thick and the coating still showed spherical growth in some locations along the CNT sidewalls

(as seen in figure 2.5), as also reported in the work of Liyanage et al. Abadi et al. also showed that Al_2O_3 thicknesses less than 2 nm, had the same deformation response as bare CNTs when loaded under flat punch indentation testing. While thicker coatings of 10 nm showed fractures of both the coating and the CNT when loaded to more than 60 MPa, demonstrating that the forest became brittle with thicker coatings. [38] Consequently it is critical to achieve conformal uniform coatings less than 10 nm on VACNT forests and to optimize the ALD process or functionalize the CNTs to attain better diffusion, adhesion, and nucleation of the deposition metal. This would allow us to fabricate a controllable conformal oxide coating along individual CNTs in a VACNT forest which could then be used to measure thermal and electrical transport properties.

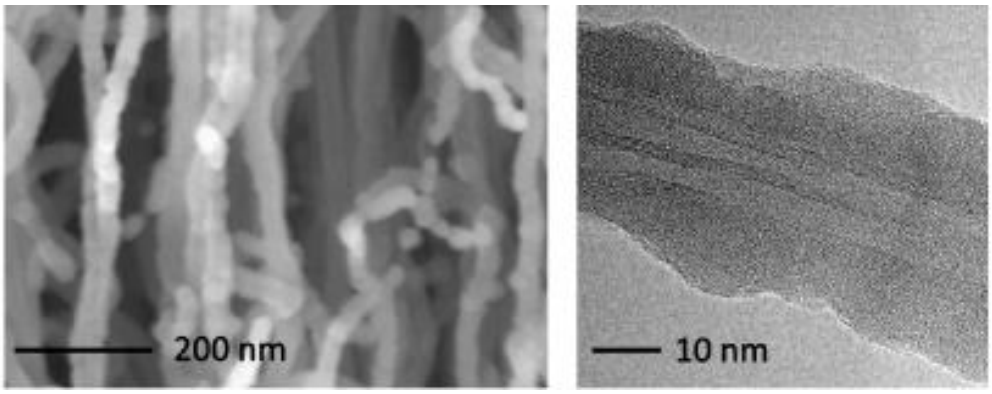

Figure 2.5 Vertically aligned multiwall CNT forests coated with Al_2O_3 by atomic layer deposition

3. EXPERIMENTAL METHODS

The following sections describe the tools and methods used for fabrication processing and characterization our oxide-coated vertically aligned carbon nanotube (VACNT) forests.

3.1 Processing

3.1.1 CNT Growth

The VACNT forests were grown using an Aixtron Black Magic chemical vapor deposition (CVD) system. CVD is a controllable growth process for vertical CNT alignment that uses hydrocarbon gases as the carbon source.[39] Figure 3.1[40] is a schematic of the multiwall CNTs (MWCNTs) growth process using CVD. It has two growth types: root growth, where the CNT grows on the metal particle, or tip growth, where the CNT grows while carrying the metal particle to the top of the forest. Growth begins by decomposing the hydrocarbon and dissolving the carbon in the hot metal catalyst. Then the metal particle is saturated, and crystallization is initiated, forming cylindrical walls from the carbon to make up the MWCNT. Iron is used as the transition metal, since it is capable of decomposing gas molecules containing a carbon source used for the CNT growth.[41, 42] A high electrical conductivity (0.002-0.005 Ω·cm) Silicon substrate was used with the following catalyst stack deposited by e-beam deposition (bottom to top): 60 nm Ti, 10 nm Al, and 3 nm Fe. A low-pressure chemical vapor deposition (LPCVD) technique was used with a growth temperature of ~750°C, chamber pressure ~10 mbar, and acetylene precursor for carbon. A growth time of 60 seconds was used to achieve forest heights of 10-14 μm. Longer growth times were used for taller VACNTs used in studies as a function of array height. Heights of CNT forests were verified using a Zeiss Ultra60 field emission scanning electron microscope (SEM), at an accelerating voltage of 5 keV.

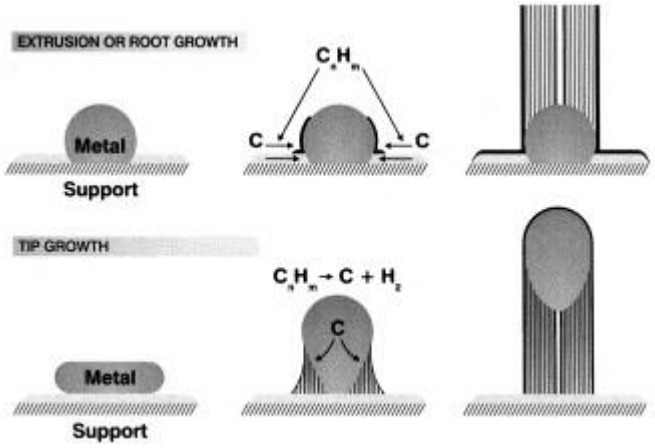

Figure 3.1 Multiwall carbon nanotube growth process by chemical vapor deposition

3.1.2 Atomic Layer Deposition

A Cambridge NanoTech atomic layer deposition (ALD) system was used for our plasma-enhanced atomic layer deposition (PALD), where oxides were deposited on individual CNTs in forests. This process was facilitated by O_2 plasma pretreatment to functionalize the surfaces of the CNTs to nucleate oxide growth.[43] Atomic layer deposition is a well-established process, with many excellent reviews in the literature.[31, 36, 37, 44-46] Briefly, ALD controls film thickness to as fine as 0.1 Å per cycle by breaking the CVD reaction into two half reactions. The precursors are kept separate by pulsing the first precursor into the system followed by a pulse of inert gas such as Argon to purge the system, then the second precursor is pulsed and an Argon purge follows again. ALD has the advantage of coating high aspect ratio surfaces[31] such as CNTs in forests, but it has a relatively slow deposition rate.[37]

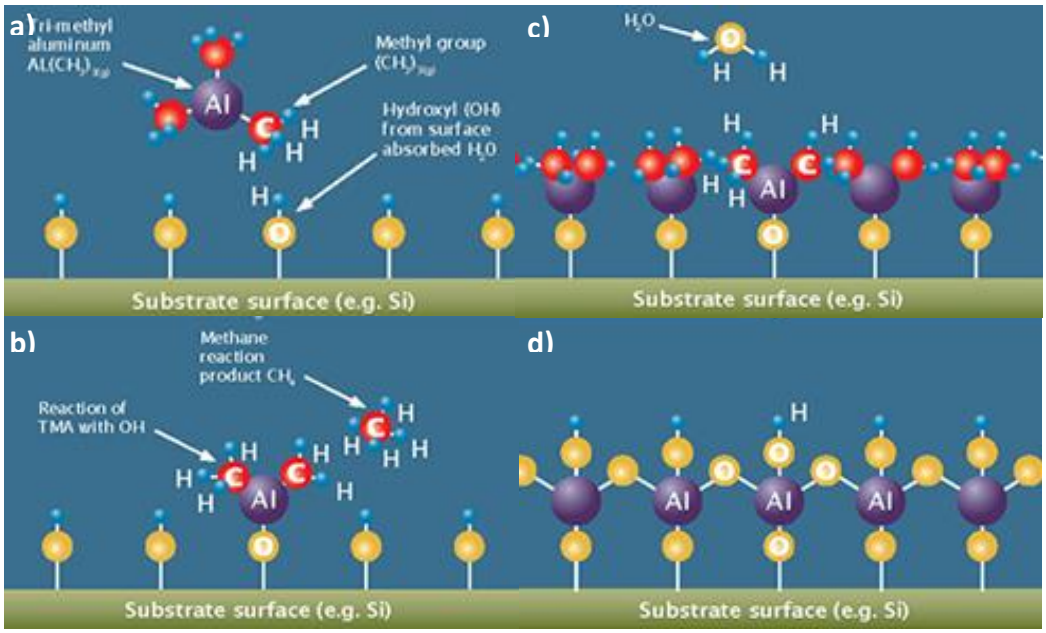

Figure 3.2: Al_2O_3 atomic layer deposition process schematic

(a) Water is pulsed and absorbed onto the surface forming a hydroxyl group, followed by a TMA pulse (b) TMA reacts with adsorbed with hydroxyl groups until passivized and methane is the reaction product (c) Excess precursor and methane is pumped away, and water is pulsed again (d) Water reacts with dangling methyl groups and forms first layer of Al_2O_3 plus hydroxyl surface groups.

Oxide coatings deposited by ALD on vertically aligned carbon nanotube (VACNT) forests in this work include: Al_2O_3, AlN, Pt, and ZnO. The precursors for Al_2O_3 are trimethylaluminium (TMA) for Aluminum and H_2O for Oxygen. Al_2O_3 is deposited thermally at 250°C with a deposition rate of 1.0 Å - 1.1 Å per cycle and 30-second exposure times. A schematic of Al_2O_3 deposition in ALD is shown in Figure 3.2[47]. ZnO precursors were Diethyl Zinc (DEZ) for Zn and H_2O for Oxygen. ZnO was deposited thermally at 250°C with a deposition rate of 1.2 Å per cycle and 30 second exposure times. AlN precursors are trimethylaluminium (TMA) for Aluminum and N_2 plasma for Nitrogen. AlN was deposited by plasma at 250°C at a rate of .98 Å per cycle and 30 second exposure times. Pt precursors are (Trimethyl) methylcyclopentadienylplatinum (IV) for Platinum and O_2 plasma for Oxygen. Pt used plasma deposition at 250°C with a deposition rate of 0.60 - 0.65 Å per cycle and 30 second

exposure times. Oxide thicknesses deposited ranged from 0.2 nm to 15 nm with a pretreatment of O_2 plasma for duration of 1minute at 300 W and 20 sccm.

3.1.3 Thermal Treatment

We thermally treated a bare CNT forest and two Al_2O_3 coated forests of 0.5 nm and 15 nm thick to study the chemical stability of a CNT forest with and without a coating. Thermal treatment was completed in a 3-zone Lindberg tube furnace, which has a maximum temperature of 1100 °C. The treatment was done with the tube in an ambient air environment for 100 hrs. The ramp rate on the furnace was set to 3 °C/minute, and it stayed within ±5 °C of the set point temperature. Two sets of treatments were completed; the first was done at 200 °C since CNTs are typically chemically stable in air up to about 450°C. The second treatment was done at 600 °C in air, when CNTs become reactive towards oxygen and have been shown to lose about 90 % of their original weight percentage.[23]

3.2 Characterization

3.2.1 Raman Spectroscopy

In this study we quantitatively look at the purity of our CNT forests by the D/G intensity ratio extracted from measured Raman spectra.[48, 49] The D/G ratio stems from CNTs composition of sp^3 bonds found in diamond (D) and sp^2 bonds found in graphite (G). The D band is generally viewed as a defect in MWCNTs[50], which leads to less energy transport across the material. Thus a ratio less than 1 suggests a higher quality, or graphitization of CNTs, whose molecular structure is closer to that of graphitized carbon. In MWCNTs the D and G bands are visible as they are in graphite.[51] The D band has a peak frequency at ~1326 cm^{-1} and the G band's peak frequency is ~1580 cm^{-1}.[51, 52] The G-band originates from sp^2 C-C bond stretching, which typically splits into two modes in SWCNTs: the G+, which arises from axial C-C vibrations and the G- which arises from circumferential C-C vibrations. The D-band however, is due to defect sites. [52]

Raman spectra are obtained by illuminating a sample with a laser to inelastically scatter phonons; this results in a shift in the energy of the emitted photon, which is known as a Raman Shift. Our Raman instrument is a Renishaw Raman microscope (RM 1000); the excitation source is an Argon ion laser excitation of 514 nm. Figure 3.3[53] is a schematic of the Raman spectra collection process. The Argon laser is incident on the sample, where the majority of light is scattered elastically and blocked by a filter. A CCD camera then detects the inelastically scattered photons, and the relatively weak Raman wavelength is recorded. The experimental uncertainty was determined by taking three measurements in different spot locations per sample and then solving the standard deviation between those measurements. Our experimental uncertainty was within ± 16 % for the calculated I_D/I_G ratio.

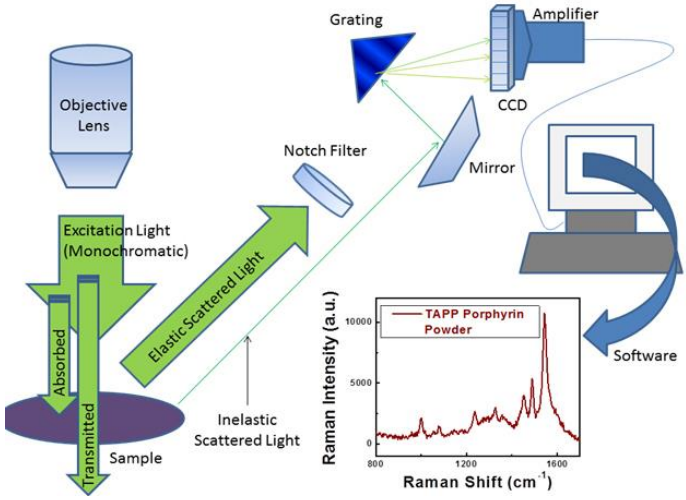

Figure 3.3: Schematic of raman spectra process

3.2.2 X-ray Photoelectron Spectroscopy

X-ray Photoelectron Spectroscopy (XPS) is used in this study to understand the nature of chemical bonding. XPS is a surface sensitive quantitative technique that also measures elemental composition.[54] This allows us to observe carbon and oxygen bond types, as well as to verify the existence of elements within a sample. XPS spectra are obtained by irradiating a material with a beam of X-rays, while measuring both the kinetic energy of the electron and electron count for

electrons that escape the top ~8 nm. The binding energy is calculated with the following conservation of energy equation:

$$E_{BE} = E_{photon} - (E_{Kinetic} + \phi), \quad \text{Eq. 3.1}$$

where E_{BE} is the binding energy (BE) of the emitted electrons, E_{photon} is the energy of the X-ray photons being used, $E_{Kinetic}$ is the kinetic energy of the electron as measured by the instrument, and ϕ is the work function, which is essentially an instrumental correction factor that accounts for the small amount of energy given up by the photoelectron as it is absorbed by the detector. Each element produces a set of characteristic XPS peaks at specific binding energies that directly identify the element. The electron counts are measured as counts per second to correlate the intensity of the various elements within the top few nanometers of the material. A gold film of 30 μm on Si was used to calibrate the system. The experimental uncertainty was determined by taking three measurements in different spot locations per sample and then solving the standard deviation between those measurements. Our experimental uncertainty was within ± 3.07 % for each element atomic percentage measured.

3.2.3 X-Ray Diffraction

X-ray diffraction is used to analyze the crystallinity and orientation of the oxide coatings on the VACNT forests.[55] This work was completed using a PAN analytical (X'Pert-Pro) diffractometer with $CuK_{\alpha 1}$ radiation of wavelengths 0.1541 nm and $CuK_{\alpha 2}$ radiation of wavelengths 0.1544 nm. The bare CNT forests and oxide coated samples were emitted with an intensity ratio of 2:1, a voltage of 45 kV and current of 40 mA. The step scans were performed for 2θ = 8°- 85° with a step width of 0.008° and a scan speed of 1s. The XRD spectra are collected from x-rays that diffract from crystalline atoms. The diffracted beam angles and intensities are then measured and a crystallographer takes the 2-D image of the diffraction pattern (raw data) and converts it by a Fourier transform into a 3-D model of the density of electrons (real space) within the crystal. A sharp peak tells us the material has a crystal structure while a flatter peak tells us it is amorphous. The mean positions of the atoms in the crystal are

determined from the electron density.[55] The experimental uncertainty was not quantified in this study; since only the peak locations were identified, a minimum of three scans were performed on a single sample.

3.2.4 Modified Photoacoustic Technique

A modified photoacoustic (PA) technique was used to quantify thermal performance by measuring the total resistance and effective thermal conductivity of both pristine (as grown CNTs) and oxide-coated VACNT forests. The PA technique is preferred over traditional steady-state thermal resistance characterization tools such as 1-D reference bar because of the ability to extract thermal parameters such as thermal conductivity, contact resistance and layer resistance. It also provides controlled repeatable measurements with a controlled pressure cell but we must note that there are variations in contact area and effective density of the grown CNT forest which is discussed as needed throughout this thesis. A modulated laser beam (λ=1100 nm) irradiates the sample within a helium filled cell. Helium is used because of its high thermal conductivity, which produces the best signal-to-noise ratio. As the sample surface is heated, helium in the cell expands, creating a periodic temperature-induced pressure response in the acoustic chamber. This creates a pressure wave (sound) that is then detected by a microphone embedded in the chamber wall. Frequencies range from ~ 10^2 to 10^4 Hz in our measurements, which penetrates different depths of the sample and maps the thermal resistance through these depths. A lock-in amplifier extracts the phase shift of the microphone relative to the heating pulse (frequency). We use the set frequency and measured phase to fit for the unknown thermal properties in the stack a model based on 1-D heat conduction in a multilayer material with modulated incident light.[56, 57]

For total resistance measurements, a 25 μm thick silver foil (99.998%, Alfa Aesar, Inc.) is placed in contact with the VACNT forest free tips as a dry contact as seen in figure 3.4a.[58] The silver foil serves as a thermally-thin top substrate due to its high thermal conductivity ~430 W/m-K. The silver foil is coated with 80 nm of titanium by e-beam evaporation to absorb the laser energy. PA measurements were performed over a pressure range of 30 - 140 kPa being

applied to the CNT tip interface (by controlling the chamber pressure). This allowed us to study the pressure dependence of the thermal interface resistance. For bare measurements, the silver foil was removed and the oxide-coated VACNT forest was the top substrate as seen in figure 3.4b. Overviews of the PA technique, the underlying theory, and its capabilities can be found in references.[56-58] Figure 3.5 is a schematic of the PA setup in the nanoengineered systems and transport lab at Georgia Tech.

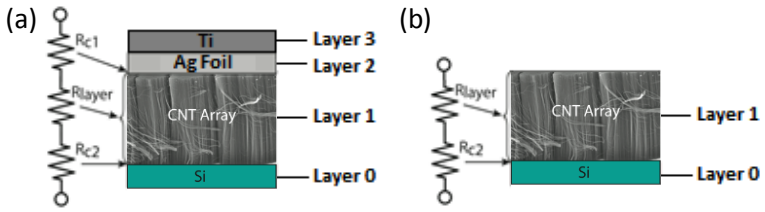

Figure 3.4 Sample configurations with relevant resistances and fitted layers (a) total resistance measurement stack (b) thermal conductivity bare measurement stack

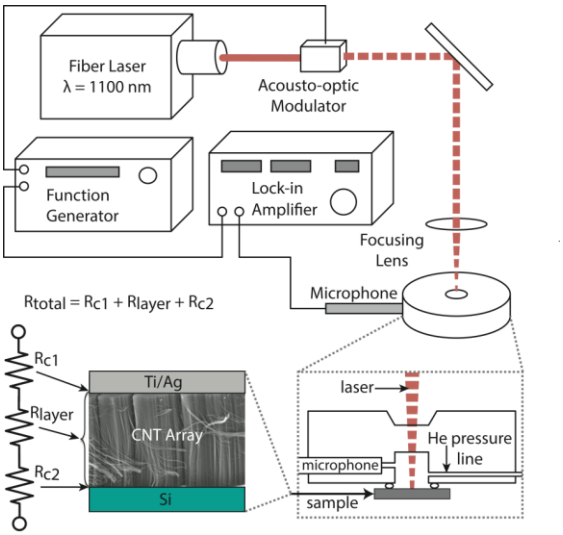

Figure 3.5 Schematic of modified photoacoustic system

The experimental uncertainty was determined by taking at least two measurements in different spot locations per sample and then fitting the data and selecting a minimum of five fits (or residuals) per measurement and then combining the standard deviation between those fits. Our experimental uncertainty was within ± 28 % of the fitted thermal conductivity measurement and ± 26 % of the fitted total thermal resistance measurement. A sensitivity analysis was also completed where sensitivity is defined as:

$$S_i = p_i * (\partial\varphi/\partial p_i) \quad \text{Eq 3.2}$$

where p is the value of property i, φ is the phase shift.[59] Sensitivity was plotted for all the fitted parameters in the measurement. The plot was used to study trends and to verify that the bare measurements were significantly more sensitive to the thermal conductivity of VACNT layer than the total resistance measurements.

3.2.5 Electrical Resistivity Measurements

Using a two probe technique, electrical resistivity measurements were made on bare and coated vertically aligned carbon nanotube forests, to measure changes in resistance. For the first technique, an HY3002 dc-regulated power supply was connected to a 4-point Signatone probe station. We used SE-20TB signatone probes, 20 μm in diameter with the Signatone micromanipulators. The VACNTs were grown on silicon substrates with a resistance of 0.001-0.005 Ω·cm. Resistivity measurements were made by recording the voltage output and induced current of the various Al_2O_3 coated samples across a specified area. Measurements are sensitive to separation distance between the two probes and to the pressure applied. Thus the probes were measured to have the same separation distance of 12 mm for each measurement. The measurement was completed by placing 1 probe in contact with the top of the silicon substrate and then closing the circuit with the opposing probe so as to apply a minimum amount of pressure each time. A minimum of 3 measurements were taken per sample; each measurement averaged 5 data points taken. The experimental uncertainty was determined by taking the standard deviation of the 3 measurements.

Layer resistance is measured by applying a titanium/gold (Ti/Au) coating, which creates a controlled top surface and increases conduction through the forest; this method has been practiced in prior measurements done on VACNTs.[60, 61] Differences in layer resistance are measured by coating our bare and oxide coated samples with 80 nm of titanium, followed by 250 nm of gold deposited with a Denton e-beam evaporator. One probe was placed on the top surface of the Au while the other was placed on the top surface of the silicon substrate as seen in figure

3.6a. This method eliminates any contact resistance on the top surface, and although we cannot extract an exact layer resistance due to the Ti/Au layer, this gives us a better understanding of the layer resistance value and how contact resistance plays a role. The experimental uncertainty fell within ± 36 % of the measured electrical resistance measurement.

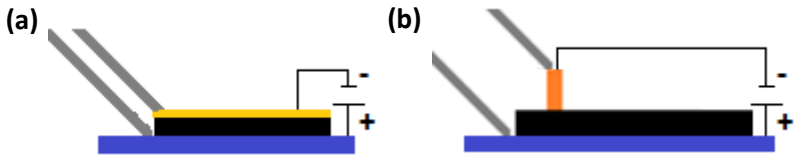

Figure 3.6 Schematic of probe placements for electrical (a) layer resistance measurement and (b) total resistance measurement

The second measurement technique was used to study the total resistance of our sample when in contact with a top metal surface as shown in figure 3.6b. We used ultra-conductive copper (Alloy 101) as a means to minimize and eliminate the resistance of the metal, which we calculated to be 2.54E-06 Ω. The weight of the copper block was equivalent to ~138 kPa in order to mimic the pressure during the total resistance measurements. These contributions do not allow us to extract layer resistance, but they allow us to study the effect that contact resistance and pressure play on the overall total measurement. The experimental uncertainty fell within ± 38 % of the measured electrical resistance measurement. The two techniques produced essentially the same uncertainty between the three measurements taken per sample, this is likely attributed to having a controlled contact surface in both the Ti/Au coating and copper block.

4. FABRICATION AND STRUCTURE OF OXIDE-COATED CNTs

This chapter discusses the fabrication and characterization of various oxide-coated CNT forests and justifies the various processing steps taken. Of the various oxide coatings attempted, only aluminum oxide (Al_2O_3) coated CNTs were characterized for thermal and electrical performance, and chemical robustness. This was because Al_2O_3 achieved a conformal uniform oxide coating along the CNT sidewalls, which is discussed further in Chapter 4.2.

4.1 Plasma Treatment of Carbon Nanotubes and Chemical Characterization

Pristine carbon nanotubes, as grown by low pressure chemical vapor deposition, are hydrophobic in nature and thus do not allow uniform nucleation of oxide precursors. In order to achieve conformal oxide coating along the CNT sidewalls, hydrophilic defects must be introduced along the CNT sidewalls. For this purpose, we used in-situ oxidation of CNT surfaces using remote oxygen (O_2) plasma treatment in a perpendicular flow Cambridge ALD system, where the plasma is introduced from the top of the reactor and flows downwards perpendicular towards the substrate.[43] This process does not affect the structural arrangements (vertical alignment) of the CNT forest. Figure 4.1a shows a pristine CNT and Figure 4.1b shows the CNT after plasma treatment where substitution defects are formed. Sites where C-C bonds are broken by O_2 plasma treatment are then occupied by a host oxygen that forms nucleation sites which include carbonyl and carboxylic acid groups; where hydrogen in the system is obtained from water moisture or hydrocarbons found in the CNTs from the growth precursor[40].

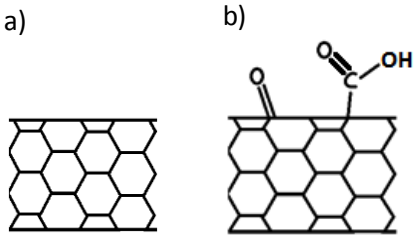

Figure 4.1: CNT cartoons (a) pristine CNTs after growth (b) plasma treated CNTs

A major concern amongst researchers is that functionalization of CNTs could significantly degrade their quality, hindering thermal and electrical transport.[62] Raman spectroscopy is widely used to study the quality of carbon nanotubes by measuring the intensity of the G-band (1582 cm^{-1}) and the carbon material disorder induced D-band (1350 cm^{-1}).[63] It is common to compare the ratio intensities of these peaks (I_D/I_G), to determine the relative defect content. Broadening of the D-band relates to the functionalization of CNTs, where sp^2 hybridized C-C bonds are converted to sp^3 hybridized C-X bonds where X may be a functional carbonyl or carboxylic acid group.[63] Raman spectra were collected to quantify the impurities in the CNT forest and any changes in CNT quality. Various plasma treatment conditions were tested, which include laser powers of 100 W and 300 W, O_2 flow rates of 20 sccm and 100 sccm, and duration of plasma treatment ranging from 1 minute to 5 minutes. The results in figure 4.2 suggest that plasma treating does damage the MWCNT structure slightly, but exposing them to plasma for longer periods of time, higher O_2 flow rates, or higher power settings does not further damage the integrity of the MWCNT structure. The I_D/I_G ratios were 0.73 and 0.85 for pristine VACNT forests and the average plasma treated VACNTs, respectively.

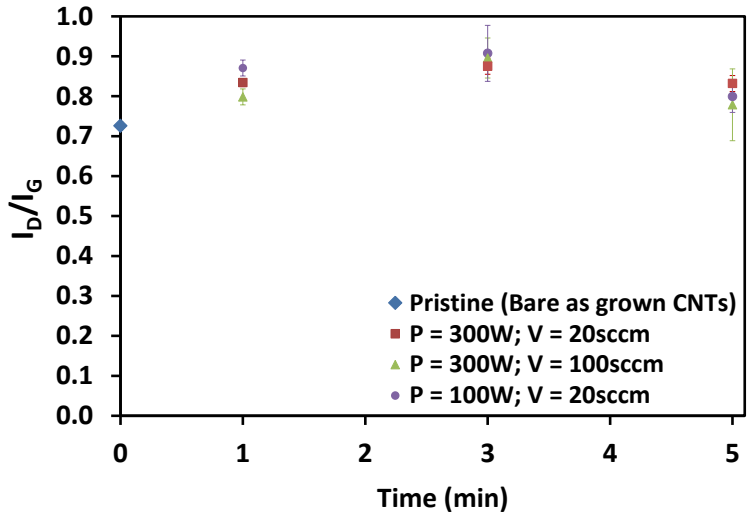

Figure 4.2 Raman spectra of varying plasma treatment parameters: time, power (P), and O_2 flow rate (V); uncertainty details may be found in Chapter 3.2.1

XPS measurements were also performed to compliment the quantitative plasma treatment impurity analysis and quantify the atomic percentage in carbon and oxygen. Figure 4.3 shows that an increase in duration of plasma treatment, power, or O_2 flow rate all result in a slight decrease in carbon percentage and consequently an increase in oxygen as shown in figure 4.4. An O_2 flow rate of 100 sccm had the greatest impact on introducing oxygen defects, but the increase in power didn't directly increase oxygen defects.

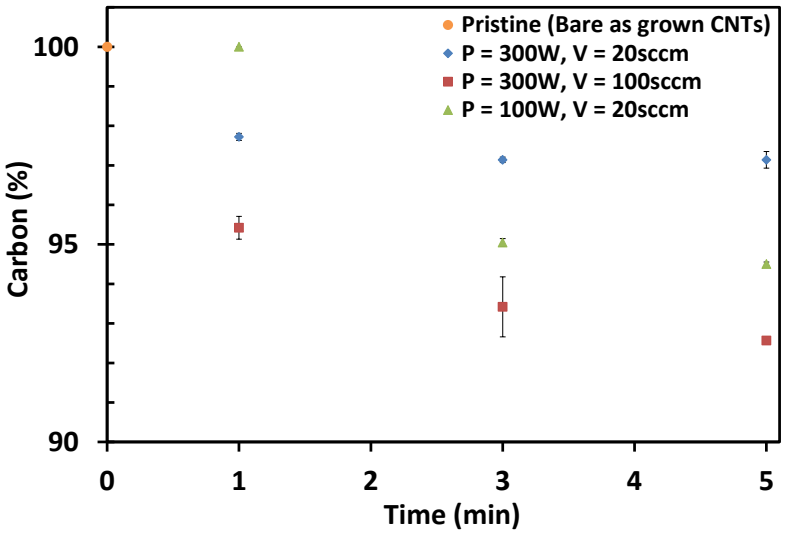

Figure 4.3 X-ray photoelectron spectroscopy carbon percentage measurements of varying plasma treatment parameters; uncertainty details may be found in Chapter 3.2.2

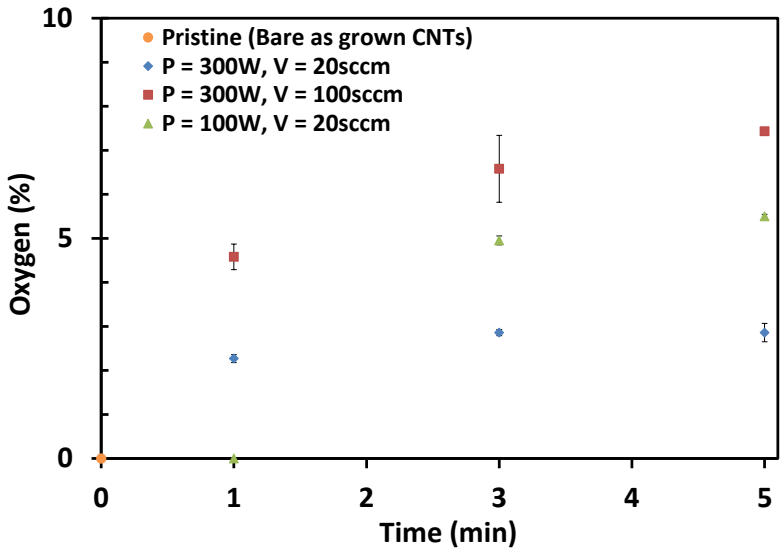

Figure 4.4 X-ray photoelectron spectroscopy oxygen percentage measurements of varying plasma treatment parameters; uncertainty details may be found in Chapter 3.2.2

Since oxygen content increases with extended durations of plasma treatment but the I_D/I_G ratios remain fairly constant, we believe that only the outer most walls in the MWCNT structures are being functionalized. This could be justified by the slow diffusion rate across solids where atoms are densely packed with severely restricted mobility.[64] Diffusion is further hindered because O_2 is a much heavier and larger diameter molecule than carbon and cannot easily penetrate the CNT lattice as a result. The process of substitution diffusion is shown in figure 4.5. The rate of this diffusion depends on two key factors: the number of vacancies and the activation energy to exchange atoms with vacancies.[65] Activation energy is defined as follows:

$$E_{activation}=k_B*T \qquad \text{Eq. 4.1}$$

k_B is the Boltzmann constant and T is 250°C in our case; this is the temperature of the system during plasma treatment. Therefore, as time elapses, the activation energy remains constant and the number of substitutions increases, thus increasing the oxygen content on the outer layer of the MWCNT. We concluded that although treating the CNT forests with plasma does slightly

decay the quality of CNTs and increases oxygen content, thermal transport measurements show that is does not hamper thermal transport performance. To further support this claim, Han et al. reports that once about 1% of carbon nanotubes are functionalized, any further increase in defect density doesn't reduce the thermal conductivity.[43] .

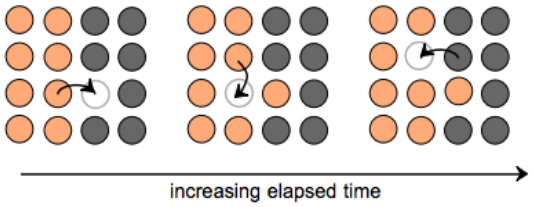

Figure 4.5 Schematic of substitution diffusion process

4.2 Oxide Coating Morphology

After the VACNT forests were functionalized, they were coated with various oxides by atomic layer deposition (as described in Chapter 3.1.). Prior work suggested that failure to functionalize CNT forests results in non-uniform thicknesses and discontinuous coatings of Al_2O_3.[38] Figure 4.6 shows top view SEM images of 8 nm thick Al_2O_3 coated VACNT forests with and without plasma treatment. The functionalization of the VACNT forests produced conformal Al_2O_3 coatings due to smooth nucleation sites (uniformly spread) along the CNT sidewalls. While the coatings were not conformal when pristine CNTs were coated due to rough nucleation sites.

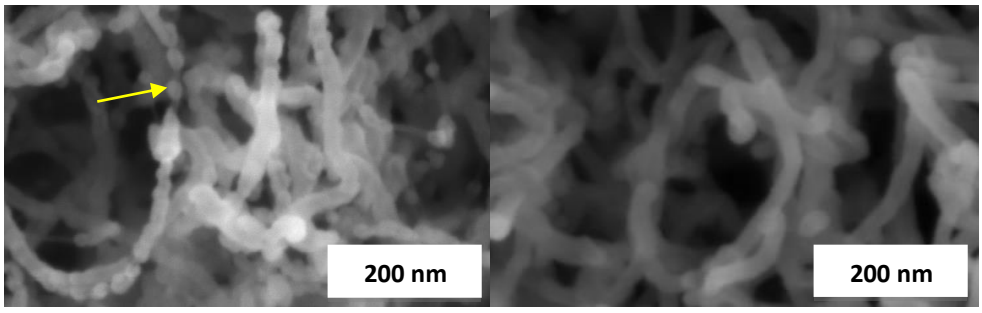

Figure 4.6 Scanning electron microscopy top view images of 8 nm thick Al_2O_3 coatings (left) no plasma pretreatment, arrow indicates agglomerates formed on CNT sidewalls (right) Plasma pretreatment

We also tried conformal coatings of AlN, ZnO, and Pt to enable different functionalities in the coated VACNTs. Figure 4.7a shows that the 8 nm thick AlN coating is not continuous, as it has points of discontinuity and appears to have non-uniform thicknesses. The 7.9 nm thick Pt coating is also not continuous, as it contains agglomerates of Pt that built up on the CNT sidewalls, shown in figure 4.7b. Figure 4.7c shows that the ZnO coating is also not conformal, as it also contains agglomerates along the CNT sidewalls. Non conformal coatings make the process of coating the VACNTs undesirable; because it is not a controllable process, it causes thermal and electrical performance to be unpredictable due to large variations in coating uniformity. It is also difficult to protect CNTs from oxidation at temperatures exceeding 450°C when the coatings are not conformal. For applications such as high k-dielectrics, controlled uniformity coatings are required in order to realize exceptional gate control.[15] Thus we chose only to move forward with the Al_2O_3 coatings due to their promise of producing conformal coatings.

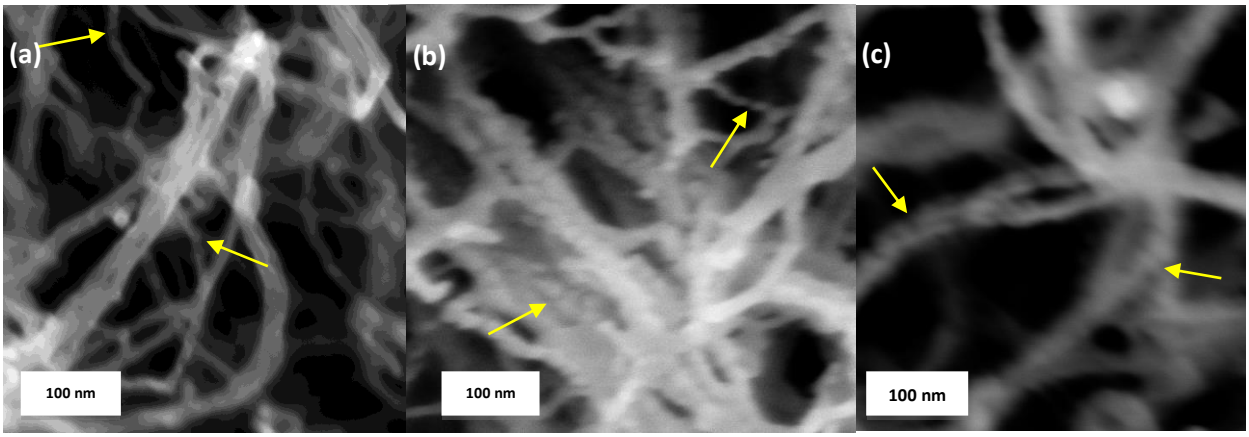

Figure 4.7 Scanning electron microscopy top view images (a) 8 nm thick AlN coating, arrows indicates locations of a non-conformal coating (b) 7.9 nm thick Pt, arrows indicate locations of discontinuity and agglomerates of Al_2O_3 (c) 9.6 nm thick ZnO coating, arrows indicate locations of agglomerates which show the coating is not conformal

Next Al_2O_3 coatings of 0.2 nm, 0.5 nm, 1 nm, 3 nm, 5 nm, 8 nm, and 15 nm in thickness were deposited. Based on SEM images, all of our oxide coatings appeared to form conformal coatings on the top layer of the forests (figure 4.8). TEM images show that oxide coatings of 15

nm have very uniform thicknesses along the MWCNT sidewalls and tip, as seen in figure 4.9. TEM images showed that coatings less than 1nm were not uniform or conformal along the entire CNT sidewalls, as shown in figure 4.10. In figure 4.10 (left) it also appears that the MWCNTs are still structurally 'soft,' as a tube in bending can be seen.

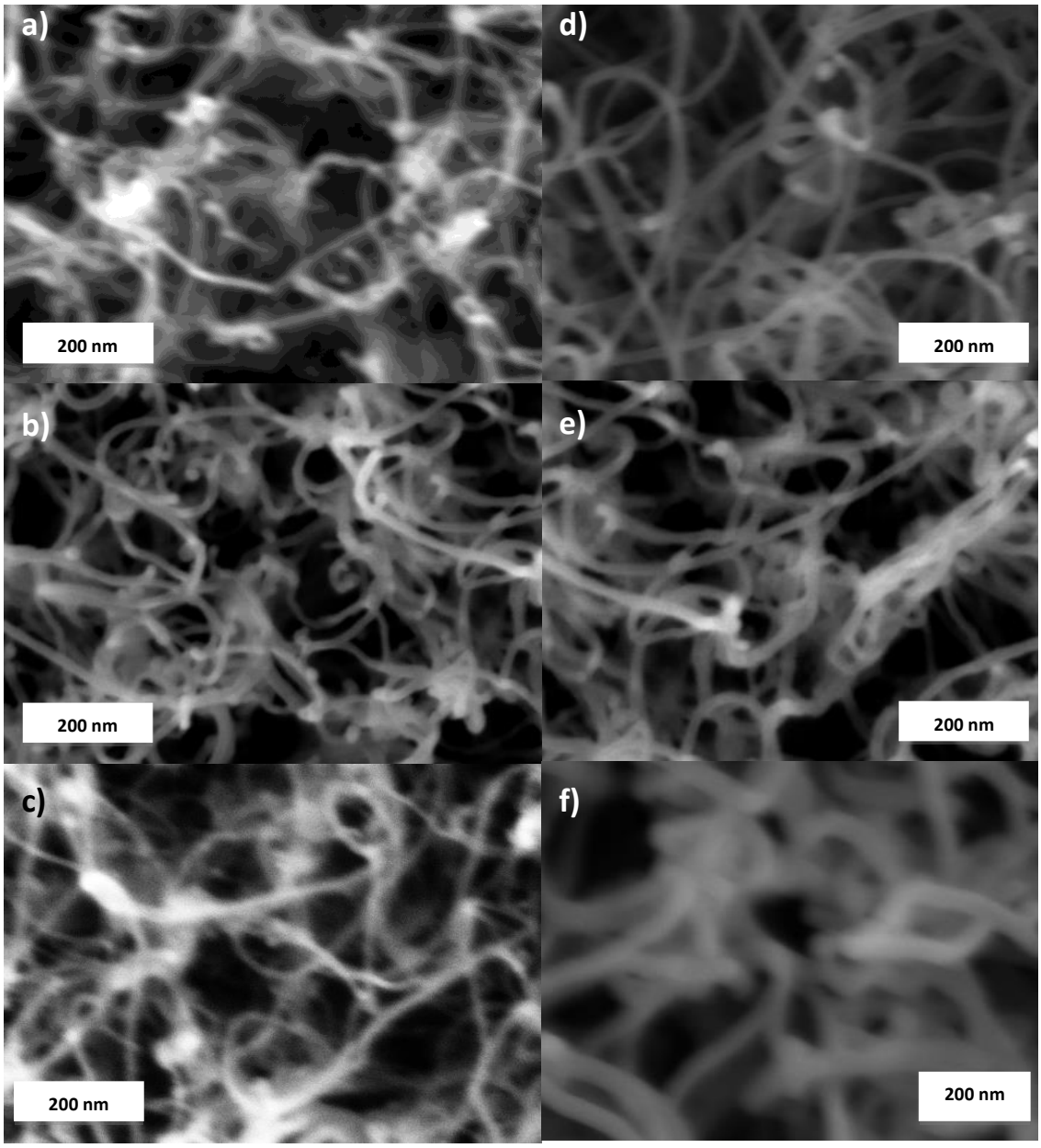

Figure 4.8 Top view scanning electron microscopy images of Al_2O_3 coatings of (a) 0.2 nm thick (b) 0.5 nm thick (c) 1 nm thick (d) 3 nm thick (e) 5 nm thick (f) 15 nm thick

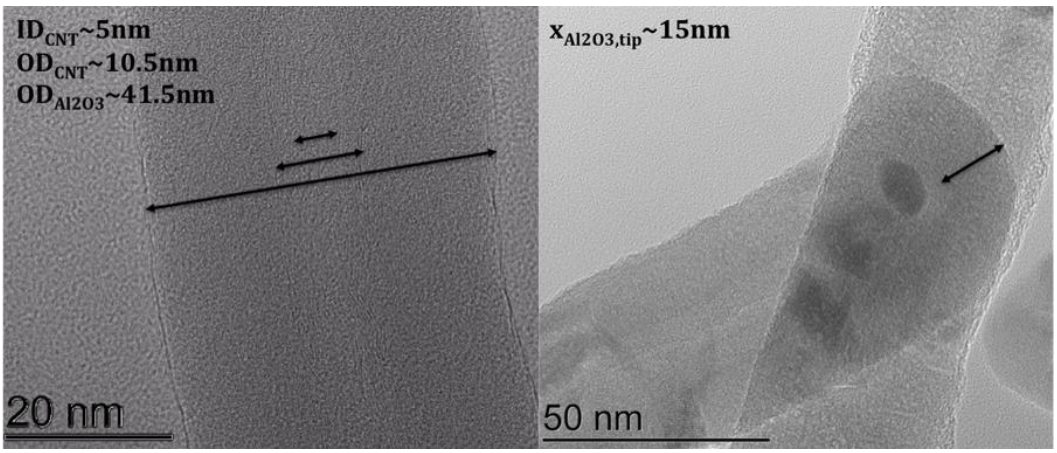

Figure 4.9 Transmission electron microscopy images of 15 nm thick Al_2O_3 coatings (left) sidewall view (right) MWCNT tip view

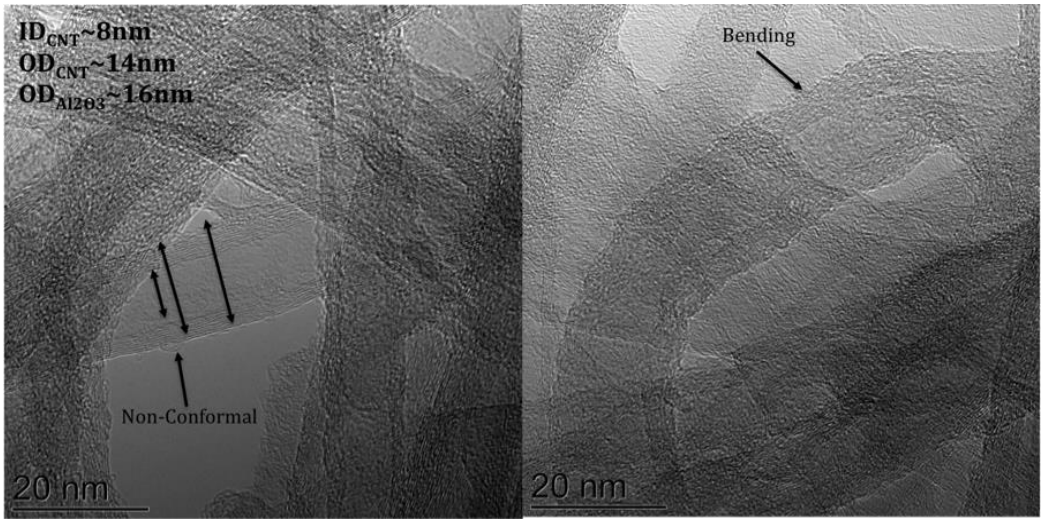

Figure 4.10 Transmission electron microscopy images of 1 nm thick Al_2O_3 coatings (left) sidewall view with non-conformal coating (right) MWCNT in bending

The conclusion that coatings less than 3 nm are not conformal is further justified by preliminary contact angle measurements taken with a Ramé-hart Model 250 goniometer, which provides automated digital contact angle measurements. Water was used a solvent since it is highly polar and VACNT forests are well known for being hydrophobic. Water has a dipole moment of ~1.85D and a surface tension in air (γ) of ~72 mN/m.[66] The contact angle measurement results are shown in figure 4.11. Coatings less than or equal to 1 nm are still extremely hydrophobic, while coatings greater than or equal to 3 nm are hydrophilic; inset SEM images show the change in top view morphology from hydrophobic to hydrophilic samples after the water droplet dried. In the bare and non-conformally coated forests (< 3 nm thick), the top

view SEM image figure 4.11a shows capillary clumping of the CNTs which suggests that VdW forces are present joining or sticking the CNTs together creating these large valleys in the top view morphology. The fact that VdW forces are present suggests there are strong inter-tube van der Waals forces present and the the MWCNTs are exposed and not conformal. The Al_2O_3 coatings less than 3 nm thick had hydrophobic behavior holding most of the water droplet above the surface as pictured in figure 4.11b. For coating thicknesses greater than 1 nm figure 4.11c shows that there was not a significant amount of capillary clumping present which suggests that the MWCNTs are no longer exposed and the VdW forces have diminished. Diminished VdW forces suggest the coatings are likely uniformly coated. These thicker coatings greater than 1 nm had hydrophilic behavior and absorbed the water droplet as seen in figure 4.11d. Accordingly we conclude that coating thicknesses greater than or equal to 3 nm are conformal.

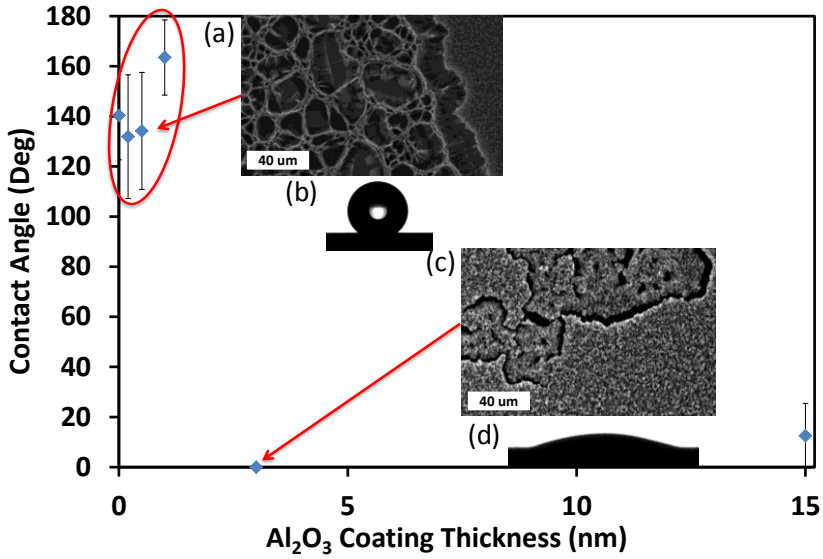

Figure 4.11 Contact angle measurements for Al_2O_3 coatings (a) top view SEM image for a 0.5 nm coated VACNT forest after water droplet placement (b) image of contact angle measurement for 0.5 nm coated VACNT forest (c) top view SEM image for a 3 nm coated VACNT (d) image of contact angle measurement for 3 nm coated VACNT forest

4.3 Chemical Characterization of Oxide Layer

A chemical characterization study was done on Al_2O_3 coated samples to study changes in VACNT forests' quality and to confirm their Al_2O_3 compositional makeup. Raman spectra were

taken for Al_2O_3 coated VACNT forests to study the effect on CNT quality by the I_D/I_G ratio. Figure 4.12 shows that the peak intensity decreases from its pristine state after O_2 plasma pretreatment, and then increases again after coating with 8 nm of Al_2O_3. Figure 4.13 shows that, as the oxide coating thickness increases to values greater than 3 nm, the I_D/I_G ratio is restored to values near to that of pristine VACNT forests. This may be attributed to Al_2O_3 coatings being conformal for thicknesses greater than or equal to 3 nm. Theoretically all defect sites (made up of double bonded Oxygen) along the surface of the MWCNT would react with the first ALD half reaction precursor H_2O to form hydroxyls (OH). Then the hydroxyls would react with the second precursor, TMA to form Al_2O_3 along the entire sidewall of the MWCNT surface. When the coatings are not conformal defect sites are still present along the MWCNT sidewalls; thus the I_D/I_G ratio is comparable to that of the O_2 plasma treated forests.

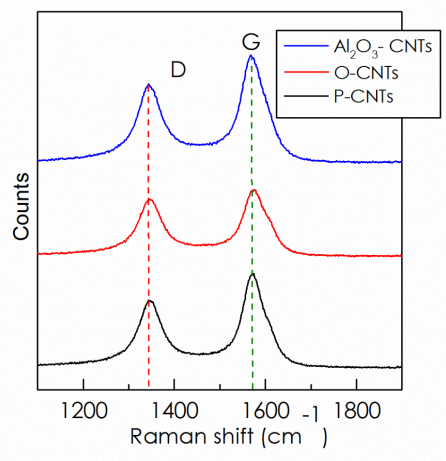

Figure 4.12 Raman spectra for pristing (P) CNTs, O_2 plasma treated (O) CNTs, and 8 nm thick Al_2O_3 coated CNTs

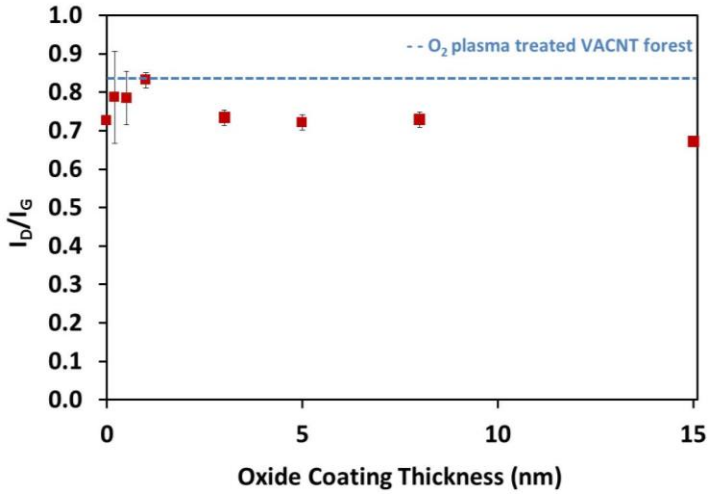

Figure 4.13 Raman results for Al_2O_3 coated VACNT forests, dashed blue line represents Raman spectra average result for O_2 plasma treated VACNT forest at 300 W of power and a 20 sccm O_2 flow rate; uncertainty details may be found in Chapter 3.2.1

XPS measurements were also performed for Al_2O_3 compositional analysis. Spectrum scans of pristine VACNT forests, O_2 plasma pretreated forests, 0.5 nm, 8 nm, and 15 nm thick Al_2O_3 coated forests are shown in Figure 4.14. O_2 plasma pretreated forests have a carbon bonded oxygen presence and a C_{1S} peak, while the Al_2O_3 coated samples show the carbon bonded oxygen as well as an Al_2O_3 presence. This stoichiometry was observed by fitting the XPS measured peak binding energies and comparing them to tabulated data in literature.[44, 67, 68] The tabulated data identifies elements by their characteristic nominal binding energies and the measured subtle but reproducible shifts in binding energy known as "chemical shifts" are then used to provide the chemical state or bonding environment.[54, 69] Table 4.1 shows the atomic percentage breakdown of elements present in the pristine VACNT forests, Al_2O_3 coated forests, and bulk ALD deposited Al_2O_3 at 15nm thick, all on a silicon substrate. The 15nm thick bulk ALD deposited Al_2O_3, shows that our ALD deposited Al_2O_3 has about a 9.4% carbon contamination. The XPS atomic percentage for commercially pure Al_2O_3 is 64% oxygen and 36% Aluminum,[70] marked on Figure 4.15, which plots the various Al_2O_3 thicknesses on VACNT forests. There is a clear trend of increasing aluminum and oxygen as oxide thickness increases. The Al_2O_3 compositional makeup does not match that of commercially pure Al_2O_3, and this is attributed to the carbon contamination of the ALD deposited Al_2O_3. Considering XPS

is only sensitive to the top 3-12 nm of a sample, the carbon contamination also explains the presence of carbon in the 15 nm thick Al_2O_3 coating where XPS is not able to detect the CNTs.

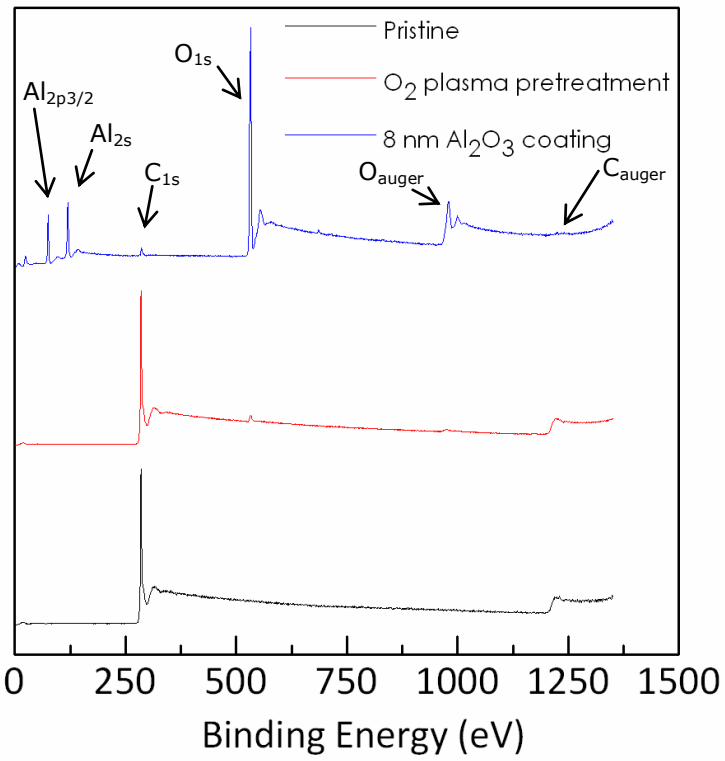

Figure 4.14 X-ray photoelectron spectroscopy for pristine, O_2 plasma treated, and 0.5 nm, 8 nm, and 15 nm thick Al_2O_3 coated forests

Table 4.1 X-ray photoelectron spectroscopy measurements for Al_2O_3 coated VACNT forests; uncertainty details may be found in Chapter 3.2.2

Sample		*%C*	*%O*	*%Al*
Pristine		100	NA	NA
Al_2O_3	15nm	4 ± 1	65 ± 1	31 ± 1
	8nm	7 ± 1	53 ± 2	40 ± 2
	5nm	6 ± 1	53 ± 1	41 ± 1
	3nm	17 ± 1	58 ± 1	25 ± 1
	1nm	70 ± 2	20 ± 3	10 ± 1
	0.5nm	87 ± 1	9 ± 1	4 ± 1
	0.2nm	92 ± 1	6 ± 1	2 ± 1
Al_2O_3 Bulk		9 ± 2	50 ± 1	41 ± 1

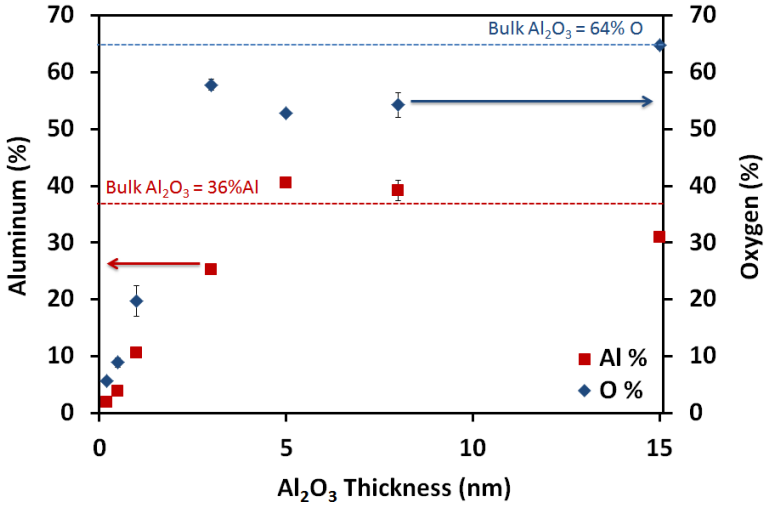

Figure 4.15 X-ray photoelectron spectroscopy results plotted for Al_2O_3 coated samples; uncertainty details may

4.4 Oxide Coatings at Different Forest Heights

All array heights in the previous sections ranged from 10-14 μm in height; in this section we investigate the maximum forest height that can achieve a conformal coating. Figure 4.16 shows, as a point of reference, what 10 μm tall bare VACNT forests look like through SEM. Figure 4.17 is an SEN image of an 8nm thick Al_2O_3 coated 10 μm tall VACNT forest, which have conformal coatings to the root. Figure 4.18 is an SEM image of an 8 nm thick Al_2O_3 coated 35 μm tall VACNT forest that has a conformal coating from the top of the forest down to the root. (Note the sidewalls of the forest are folded over slightly in figure 4.18, making them appear shorter) Figure 4.19 is an SEM image of an 8 nm thick Al_2O_3 coated 120 μm tall VACNT forests, which does not have conformal coating to the root. This suggests that with the current ALD recipe the maximum forest height that can achieve a conformal Al_2O_3 coating may be around ~30 μm.

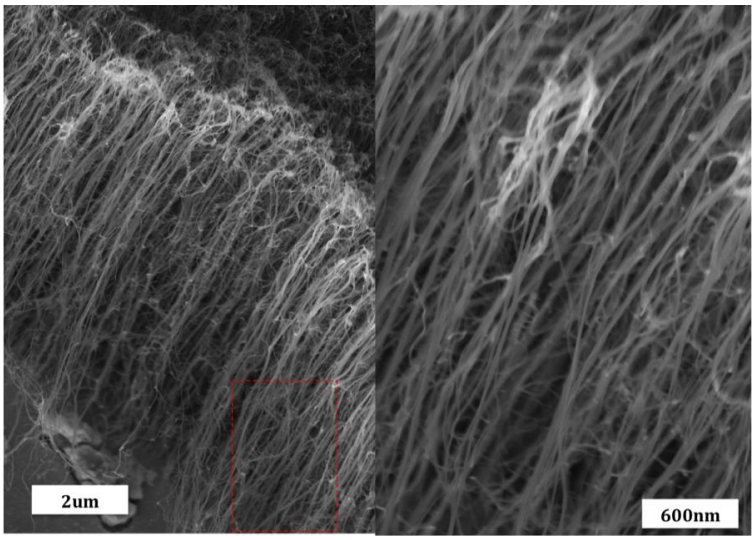

Figure 4.16 SEM images of side view pristine VACNT forests 10 µm tall, red box highlights zoomed in view displayed on right

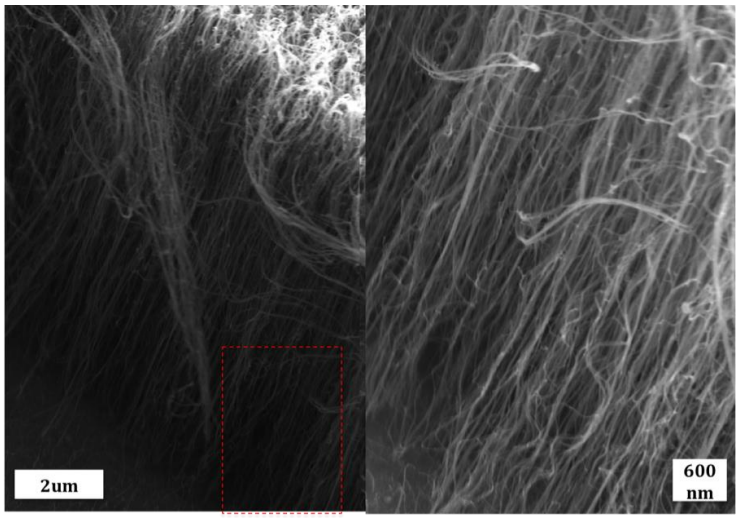

Figure 4.17 Scanning electron microscopy images of side view of 8 nm Al_2O_3 coated VACNT forests 10 µm tall, red box highlights zoomed in view displayed on right

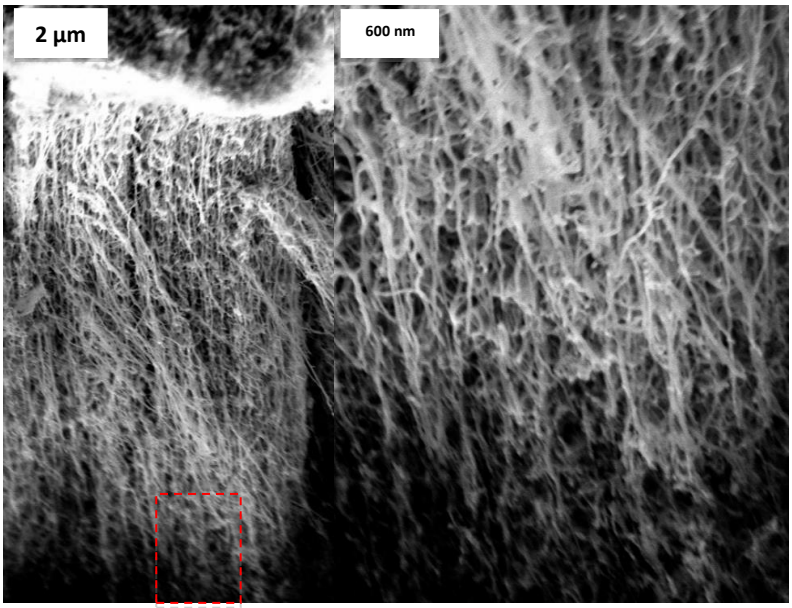

Figure 4.18 Scanning electron microscopy side view of 8 nm Al_2O_3 coated VACNT forests 35 µm tall, red box highlights zoomed in view on right

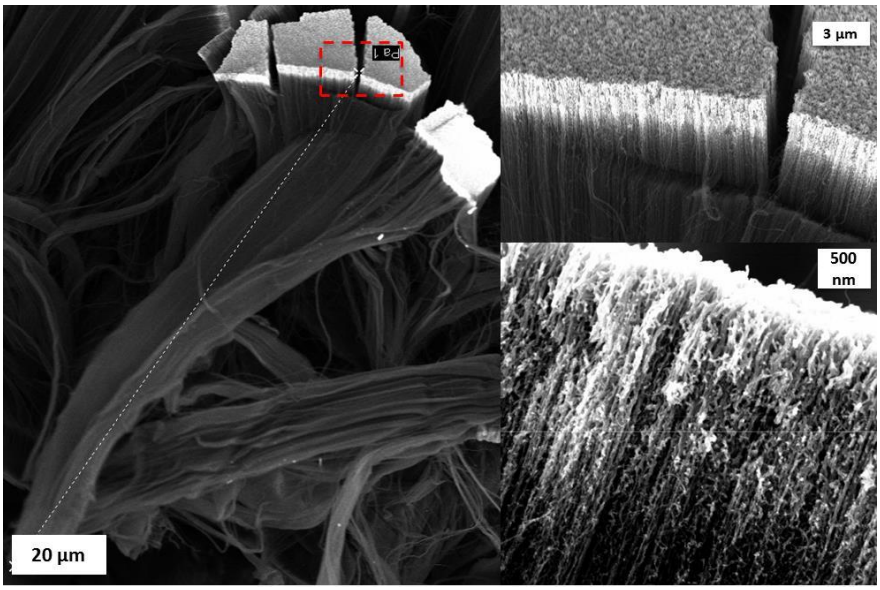

Figure 4.19 Scanning electron microscopy images of side view of 8 nm Al_2O_3 coated VACNT forests 120 µm tall, red box highlights zoomed in view on right

5. THERMAL AND ELECTRICAL TRANSPORT MEASUREMENTS

In this chapter thermal and electrical transport phenomena are explored experimentally. Thermal performance was quantified by performing two types of PA measurements to obtain the effective thermal conductivity and total thermal resistance. Electrical performance was quantified by taking 2-probe electrical resistivity measurements to obtain the total electrical resistance and layer electrical resistance. The objective of these measurements was to find an optimum Al_2O_3 thickness that gives us the best combination of high thermal conductance and high electrical resistance.

5.1 Thermal Conductivity vs. Oxide Layer Thickness

Measured values of VACNT forest thermal conductivity range from 0.5 to 267 W/mK. If only the total thermal resistance were measured, we would lack information on contributions made by contact resistance and layer resistance.[27] In order to properly study the thermal performance of our nanostructured materials, thermal conductivity measurements were made of the Al_2O_3 coated VACNT layer (referred to as VACNT layer). A modified photoacoustic technique was used to perform 'bare' measurements; further details on the modified PA technique are explained in Chapter 3.5. Bare measurements are made without a top metal foil, as shown in the inset of Figure 5.2. This eliminates an additional unknown contact resistance on the top surface and allows for a higher theoretical sensitivity to the thermal conductivity of the VACNT layer. [59] Figure 5.2 displays the measured effective thermal conductivity values of the VACNT layer across varying Al_2O_3 coating thicknesses. The thermal conductivity was relatively constant for Al_2O_3 thicknesses ranging from 0 to 15 nm. This finding agrees with our Raman measurements which indicated no change in CNT quality over the same range of Al_2O_3 coatings, and which supports the conclusion that CNT quality is not compromised during the oxide coating fabrication process. Considering the thermal conductivity of amorphous Al_2O_3 is ~1.8 W/mK[71] and the lower end for a measured individual MWCNT of 9.8 nm is ~2000 W/mK,[72, 73] applying

a rule of mixtures for a bare and 15nm Al_2O_3 coated single CNT allow us to estimate thermal conductivity values of 2000 W/mK and 501.4 W/mK respectively. If only thermal transport in the axial direction of the CNT is considered and the Al_2O_3 coated sidewalls so that only the tip is considered to be coated with 15nm, this yields no detectable effect when applying the rule of mixtures (1997 W/mK).

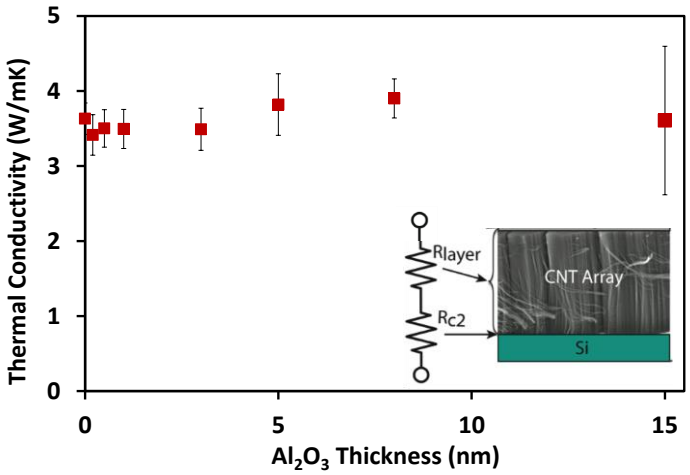

Figure 5.1 Measured effective thermal conductivity of Al_2O_3 coated VACNT layer; uncertainty details may be found in Chapter 3.2.4

In the data fitting model thermal conductivity, density, optical absorption length, and contact resistances were fit for using the Levenberg-Marquardt method, a non-linear algorithm that simultaneously fits for unknown parameters.[74] Specific heat was fixed to a value analogous to that of graphite, 700 J/kg-K.[75] The absorption length is given a range of .001-10 μm; considering that VACNTs are extremely black, absorbing more than 99% of incident light, their penetration depths are on the order of microns, while those for metal films are on the order of nanometers.[76, 77] Contact resistance from the growth substrate (Si-CNT) was set to a range of 0.05-80 mm^2K/W and that from the top VACNT layer to the He was set to 0.00001-1 mm^2K/W.[27, 58, 78] Thickness of the VACNT layer was fixed to the height confirmed in SEM for each sample. Thermal diffusivity is calculated as follows:

$$\alpha = k/(\rho \cdot c_p) \qquad \text{Eq. 5.1}$$

and VACNT layer resistance is extracted from the total resistance as follows:

$$R_{layer} = R_{total} - R_{Si\text{-}CNT} - R_{CNT\text{-}He} \quad \text{Eq. 5.2}$$

Density was given a range of 1600kg/m^3[79] a reported maximum density for VACNT forests, to 20 kg/m^3[26], which is the lower end of a previously measured value for VACNT forests using the same growth recipe. Table 5.1 summarizes the average fitted values across the various Al_2O_3 coating thicknesses.

Table 5.1 Photoacoustic thermal conductivity fitting parameters for various VACNT forest coated with varying thicknesses of Al_2O_3; specific heat and thickness are fixed while the rest of the parameters are fitted for

Oxide Coating	Therm Cond W/m-K	Density kg/m³	Spec Heat J/kg-K	Thickness µm	Therm Diff mm²/s	Layer Res mm²K/W	$R_{Si\text{-}CNT}$ mm²K/W	$R_{CNT\text{-}He}$ mm²K/W	R_{total} mm²K/W
15 nm	3.61	374.92	700	11	13.74	3.63	0.72	0.001	4.35
8 nm	3.90	104.82	700	12	53.16	3.08	0.35	0.010	3.45
5 nm	3.82	21.77	700	11	250.57	2.77	0.05	0.001	2.82
3 nm	3.86	22.00	700	11	250.65	3.50	0.25	0.010	3.68
1 nm	3.72	22.00	700	11	241.86	3.83	0.98	0.010	4.25
0.5 nm	3.66	21.74	700	11	240.50	3.84	0.97	0.010	4.27
0.2 nm	3.38	21.47	700	10	225.07	3.00	1.00	0.010	3.98
Bare	3.58	22.00	700	14	232.63	3.13	0.82	0.010	4.11

The measured effective thermal conductivity values are comparable to reported values of 2.1 to 3.5 W/mK made on SW-VACNT forests using a thermoreflectance measurement.[27] In our modified PA system we previously measured MW-VACNT forests (same recipe) of 15 µm tall at 3.8 W/mK.[59] The fitted values for density reached the lower limit of 20 kg/m^3 for non-conformal coatings (< 3 nm thick). When the densities were allowed to float down to 1 kg/m^3, the percent difference in thermal conductivity was less than 11% in all cases, with an average difference of ~4.5%. These lower fitted densities caused the thermal diffusivity to exceed the value of an individual SWCNT, ~2400 mm^2/s, which is unlikely for a forest; considering the effective density it should be an order of magnitude lower.[78] Figure 5.3 plots the calculated thermal diffusivity and heat capacity while varying density of the VACNT layer based on the PA measured effective thermal conductivity and the fixed specific heat value. The plot suggests that

our thermal diffusivity values lie in the range of reported values of 80-320 mm^2/s[58] for MW-VACNT forests and 37-90 mm^2/s[27] for SW-VACNT forests. The heat capacity values also lie in the range of a measured value of 5.2 kJ/m^3K[78] for SW-VACNT forests, to 1.5 MJ/m^3K for an individual SWCNT. As a result it is not unreasonable for our effective density to fit to below 20 kg/m^3.

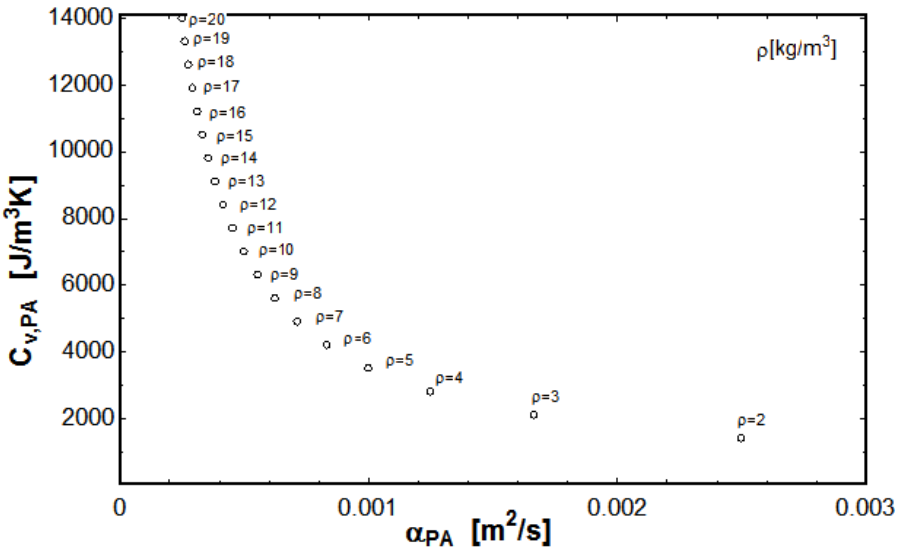

Figure 5.2 Extracted heat capacity and thermal diffusivity for varying densities

We must note that during thermal data fitting bulk material parameters are fixed, contact resistances and effective thermal conductivity of the VACNT layer are measured and effective density is given a range. Contributors to the effective density of our VACNT layer are shown in Fig. 5.1, which labels the various types of imperfections; these are described further here:

- CNT to metal contact, which does not contribute to energy transport across the interface but the CNT mass is accounted for in the measured density of the forest.
- CNT-CNT sidewall contacts reduce the theoretical conductivity of an individual CNT by altering phonon scattering.[27]
- Crystal structure defect sites lead to CNT contortion and act as phonon scattering sites, reducing the effective thermal conductivity.
- CNT pull out from the growth substrate where alignment and density are reduced affecting the estimated volume fraction (f) of the VACNT layer.[27, 78]

The measured bulk density of our forests is about 310 kg/m^3, but this includes the mass of CNTs not contributing to thermal transport. The volume fraction is often used to estimate the effective density and other unknown parameters in a MWCNT forest by comparing them to the values of individual SWCNTs. Typical values of volume fraction for MWCNT forests range from ~0.5-10%.[80]

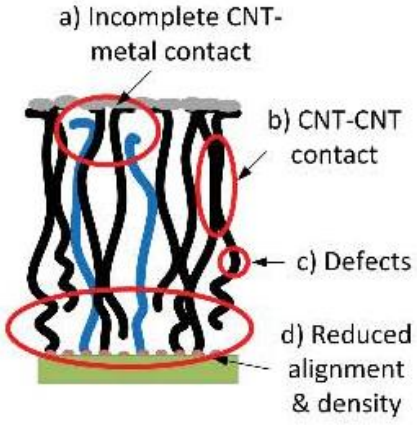

Figure 5.3 Schematic of a VACNT forest grown on Si (green) and placed in contact with a top metal (grey)

A sensitivity analysis was completed to further support our thermal conductivity measurements. Conformal Al_2O_3 coatings (i.e coating thicknesses greater than or equal to 3 nm) had very good fits, as seen in Figure 5.4, with all of the residuals being less than 0.2. Non-conformal Al_2O_3 coatings however had fits with higher residuals, less than 0.7, as shown in Figure 5.4. As a result of this increase in residuals, the sensitivity plots were studied, shown in Figure 5.5. At higher frequencies the fits are less sensitive to the contact resistance at the growth substrate (Si-res) since higher frequencies heat the top portion of the VACNT layer. Due to the minimal resistance between the VACNT layer and helium gas, the fit is not sensitive to the top contact resistance (CNT-res). This allows a relatively large sensitivity to the thermal conductivity, which is sought in a bare measurement where the top contact resistance is essentially eliminated. The fit is not sensitive to the density at the lowest frequency but becomes increasingly sensitive with increasing frequency, which correlates to the penetration depth of the laser being observed within the sample. The measured effective density of the VACNT layer

varies greatly for our bare fits, but it is not sensitive in the model, and thus has a small influence on the measured effective thermal conductivity value of the VACNT layer as described earlier.

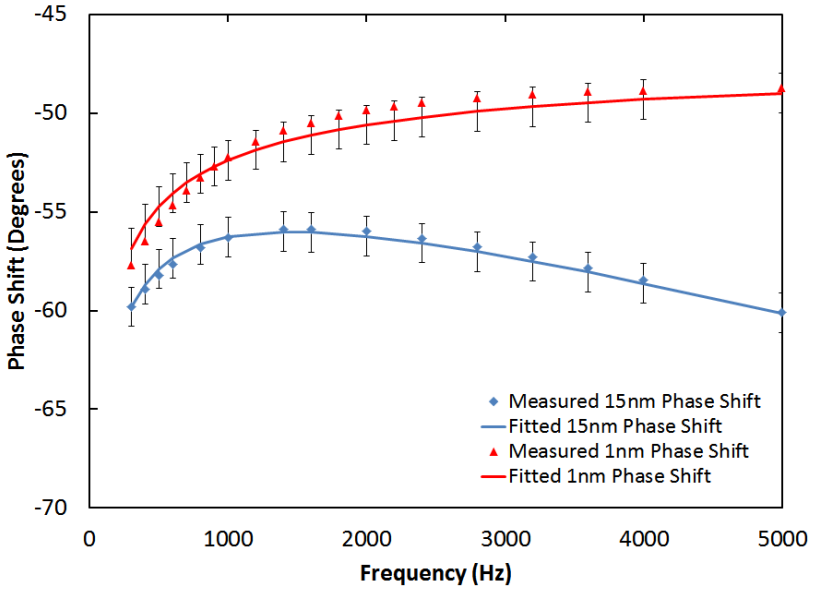

Figure 5.4 Photoacoustic phase shift fits for conformal (15 nm) and non-conformal (1 nm) Al_2O_3 coated VACNT forest with the fitted uncertainty based on ± 1 degree of the measured phase shifts

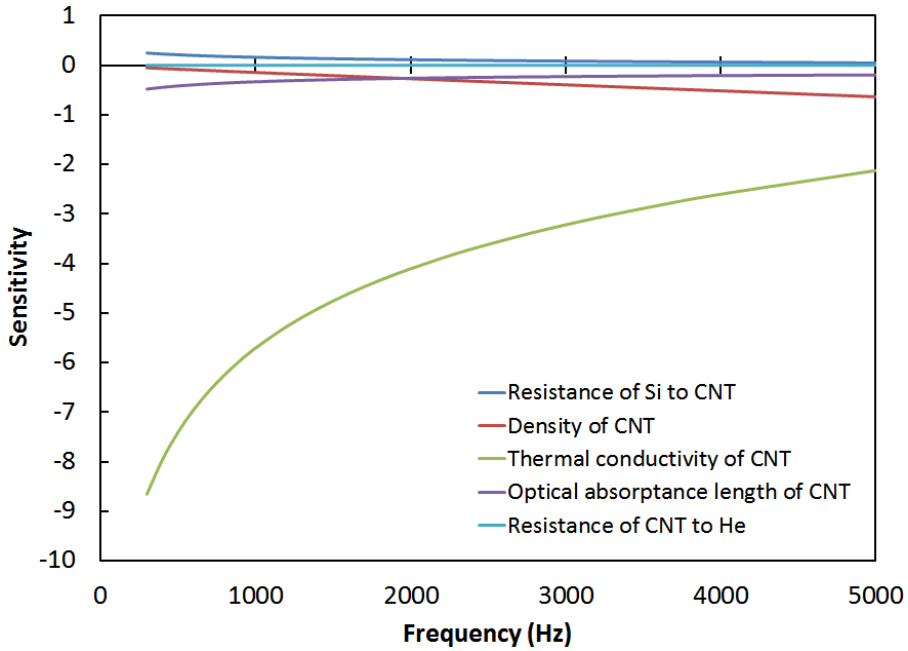

Figure 5.5 Photoacoustic sensitivity plot for conformal (1 nm) Al_2O_3 coated VACNT forests forced density >20 kg/m3

The large variability in density of our bare VACNT layer may be a result of two things. First is low sensitivity to the density as a fitting parameter as discussed previously. Second is density variability in the growth substrate due to the decay density, illustrated in Figure 5.6[81]. The CVD process starts with CNT nucleation and an activation of nanoparticles until the CNTs are dense enough to self-organize into VACNT forests. As self-organization continues, the nucleation of new CNTs continues creating shorter CNTs that do not contribute to energy transport. Density and alignment continue to increase until a peak density is reached where the highest alignment and density are achieved. Then the deactivation kinetics dominate, leading to a decay in density, alignment, and axial forces until termination of forest growth is reached. Bedewy developed a mechanical model to derive the preceding relationship between mechanical forces, CNT density, and alignment in simultaneously grown CNTs in proximity.[81]

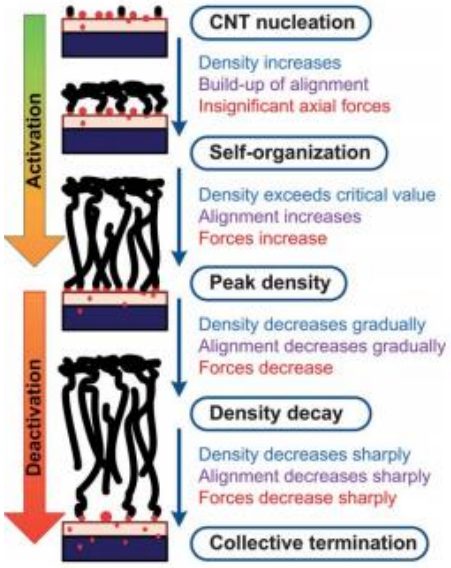

Figure 5.6 Schematic of VACNT forest growth through the evolution of density

Now we will focus our attention on the thermal transport phenomenon behind the thermal conductivity of the VACNT layer. In figure 5.7 we have plotted the thermal conductivity of an individual CNT by using the following rule of mixtures equation:

$$k_{eff,layer,PA} * f_{layer} = k_{air} * f_{air} + k_{eff,CNT} * f_{CNT} + k_{Al2O3} * f_{Al2O3} \quad \text{Eq. 5.3}$$

Tabulated thermal conductivity (k) values are used for Al_2O_3 and air, while the photoacoustic (PA) measured effective thermal conductivity is used for the forest layer. Volume fraction (f) is calculated for each parameter based on the geometry of the structure. The plot suggests that as the Al_2O_3 thickness increases, thermal conductivity of an individual CNT decreases. Considering all our VACNT forests were fabricated the same way, the thermal conductivity of an individual CNT should be unchanged. Hence our measurements do not follow the equation for rule of mixtures, so we developed a parallel resistance model to study the thermal transport across our VACNT layer.

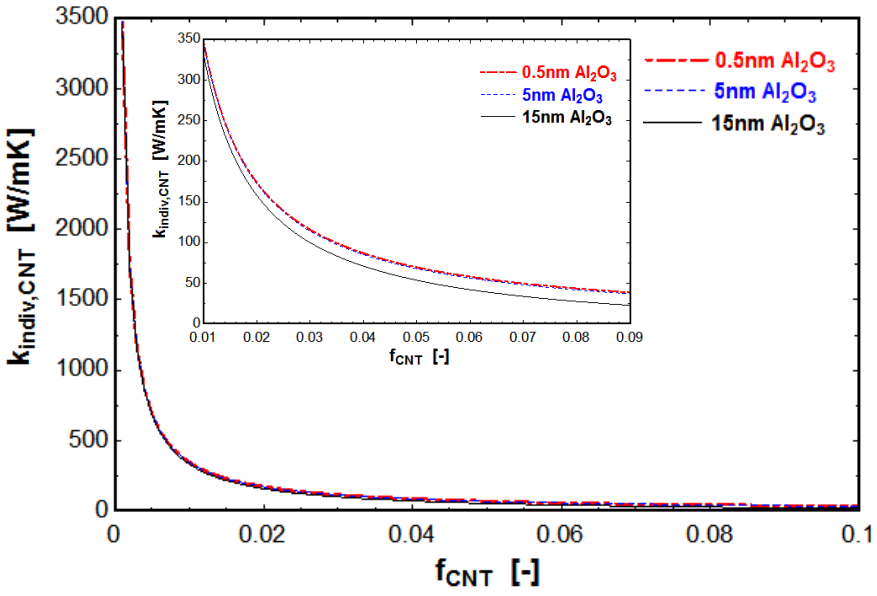

Figure 5.7 Plot of calculated thermal conductivity of an individual CNT vs. volume fraction by rule of mixtures equation

In figure 5.8, we show the resistance model that we developed for our system and the accompanying diagram. Boundary resistance at the Al_2O_3-CNT interface is neglected because scattering and coupling resistances are negligible (further discussed in Chapter 5.2) compared to the layer resistances computed. We note that thermal resistance is equal to:

$$R=L/kA \qquad \text{Eq. 5.3}$$

where k is the thermal conductivity, L is the thickness or characteristic length, and A is the cross sectional area. After calculation the R_{CNT} = 6.36 X 10^8 K/W, R_{Al2O3} = 3.14 X 10^{10} K/W, R_{Air} = 5.31 X 10^{10} K/W, and $R_{Al2O3,Tip}$ = 106 K/W. The resistance at the Al_2O_3 coated tip is so low that it does not significantly impede thermal transport. In contrast, the resistances of air and Al_2O_3 are so high that they almost block thermal transport completely, as they are two orders of magnitude higher than the resistance across the CNTs. Thus the majority of thermal energy is transported through the Al_2O_3 tip and down through the CNT as the red arrow proposes in figure 5.8. When this is assumed, the difference of total resistance calculated across the VACNT layer, R_{Total} = 6.16 X 10^8 K/W is ~3.1%. We conclude that the Al_2O_3 coating has no significant effect on the resistance of the VACNT layer, and consequently has no significant effect on the effective VACNT layer thermal conductivity value reported. Further evidence in support of this conclusion can be found in Goyny, who suggests that coating or embedding CNTs in a matrix affects the thermal conductivity of MWCNTs less than that of SWNTs because the shielded internal layers promote the conduction of phonons and minimize coupling losses.[82]

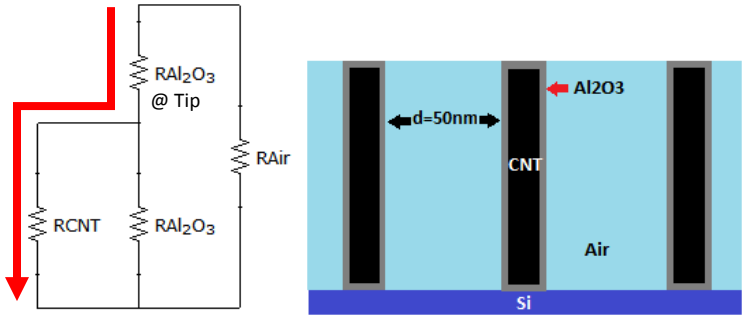

Figure 5.8 Parallel resistivity model and accompanying diagram

5.2 Thermal Resistance vs. Oxide Layer Thickness

Total thermal resistivity measurements were then made across the varying Al_2O_3 thicknesses shown in figure 5.9. In section 5.1, we found that the resistance of our VACNT layer was 2.7-3.0 mm^2K/W. Thus we can conclude that the majority of our total resistance is attributed to the dry contact interface with the VACNT forest free tips, since the contact resistance at the

growth substrate is likely near 1 mm^2K/W.[58, 78, 83] Very similar trends have been observed in previous PA studies done on MW-VACNT forests with silver foil.[58] Cola's theoretical analysis suggests that ballistic thermal resistance dominates at the CNT interface, thermal resistance is bottlenecked by the contact resistance at the free tips, and dense arrays with high mechanical compliance reduce the contact resistance by increasing contact area of CNTs with silver foil.[84]

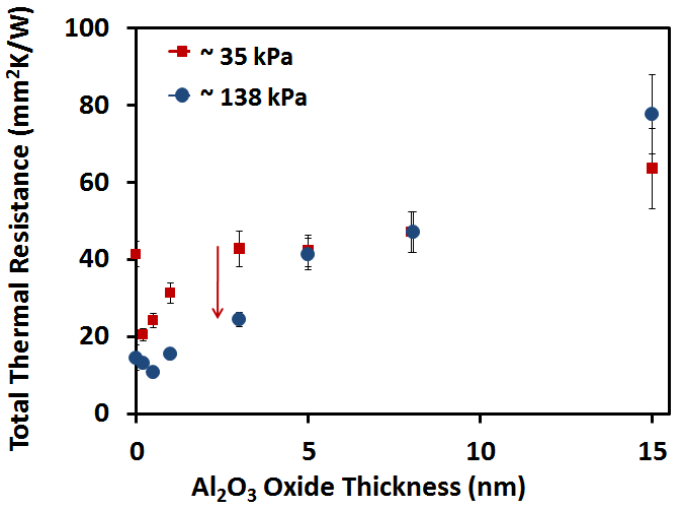

Figure 5.9 Photoacoustic total resistance measurements vs. Al_2O_3 thickness, uncertainty details may be found in Chapter 3.2.4

First we discuss what dominates resistance at the interface; ballistic transport or transport through the contact area. If transport through the contact area were dominant this would suggest that coupling effects such as electron-phonon coupling across the free tip and metal foil interface would play a role.[85, 86] Our CNT radius (b_{CNT}) is 5 nm, and, since heat transfer in CNTs is dominated by phonons, their phonon mean free path (mfp) is λ_{CNT} = 500 nm[87] near room temperature.[73] Phonons are the dominant energy carriers even at CNT- metal (silver foil) contacts, where the phonon mfp for most crystalline solids is ~100 nm.[88] Thus by calculating the Knudsen number, Kn we may determine if size effects play a significant role in contact resistance.[89] Kn is calculated as follows:

$$Kn = \lambda_{phonon}/a \qquad \text{Eq. 5.4}$$

where a is the radius of the contact size of the CNT. Cola et al. modeled the normalized CNT contact width, (a/b_{CNT}) considering elastic, radial CNT deformation as a function of b_{CNT} for the case of a CNT in contact with silver foil in air. For b_{CNT} = 5 nm, a/b_{CNT} ~ 0.15 so a ~ 0.75 nm considering the CNT radius. Thus we produce Kn values greater than unity which suggests size effects play a significant role in contact resistance and phonon transport is ballistic across a CNT-metal foil contact.[90] But the λ_{phonon} of amorphous Al_2O_3 is equal to the separation distance between atoms, which is less than 1 nm[91]; thus size effects are not dominant when coated CNTs are contacting a metal foil and transport through the contact area is dominant.

Phonons dominate thermal energy transport in ceramics (Al_2O_3) while electrons dominate thermal energy transport in metals (silver foil); thus energy transport across the interface consists of electron-phonon coupling within the metal and subsequent phonon-phonon coupling between the metal and nonmetal.[85, 86] A model developed for electron-phonon coupling within the metal suggests the resistance across the interface is dependent on thickness when accounting for size effects of the metal and non-metal layers when metal layer thickness (ℓ) is much greater than the coupling length (α), $\ell >> \alpha$. The coupling length (α) for metals is on the order of hundreds of nanometers[86] and the metal layer thickness (ℓ) is 25 μm; hence $\ell >> \alpha$. Therefore the interfacial resistance is effected by electron-phonon coupling whose resistances can range 0.001 - 0.003 mm^2K/W, which are negligible in this study when compared to the total resistance values measured.[85]

When studying total resistances at ~34.5 kPa (in Figure 5.9), the low pressure creates a large variability in the contact area, which makes it very difficult to decipher trends in the data. Although we see what appears to be a clear decrease in total resistance from bare forest measurements at 34.5 kPa to Al_2O_3 coatings less than 3 nm, we note that even if there was a change in phonon-electron coupling or phonon scattering, the order of magnitude for these effects mentioned above (~ 0.001 mm^2K/W) are negligible compared to the 20 mm^2K/W difference. A confirmation that the difference is attributed to variability in contact area is that

under ~138 kPa these Al_2O_3 coatings less than 3 nm thick have essentially equivalent total resistances to that of bare forests.

In figure 5.10 we see that as pressure increases contact resistance decreases for Al_2O_3 coatings less than 5 nm; this suggests that the forests are mechanically compliant with up to 3 nm thick Al_2O_3 coatings. As pressure is applied to the interface, the free tips are compressed, increasing the contact length of CNTs already in contact and possibly bringing more CNTs into contact with the foil (as seen in Figure 5.10a and Figure 5.10b [84]); this increases the total contact area, resulting in decreased resistance.

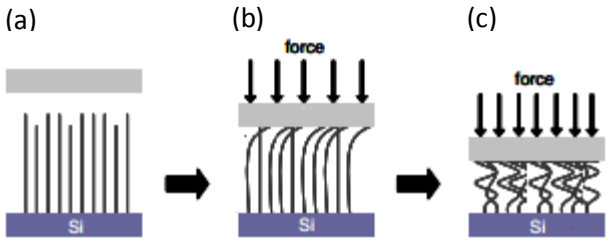

Figure 5.10 VACNT forest cartoon morphology on dependence with increasing foil pressure[84]

For the coatings 5 nm and 8 nm thick the contact resistance is the same, implying that the contact area is not increasing; thus the coated CNTs are stiff and no longer mechanically compliant. The 15 nm thick coating may or may not see an increase in resistance with pressure, considering the percent error, seen in figure 5.11. If there is an increase in resistance, we note that fracturing of the coating and CNT is not possible at a pressure of ~0.14 MPa. Fracturing would break the thermal transport path along the axial direction of the forest, which would reduce the effective density and consequently the thermal conductivity of the layer. Prior work suggests that for a 10 nm Al_2O_3 coating a minimum applied stress (σ) of ~1 MPa induces a strain (e) of 0.1 but does not lead to local buckling or fracturing along the height of the forest until it is loaded with more than 60 MPa.[38]

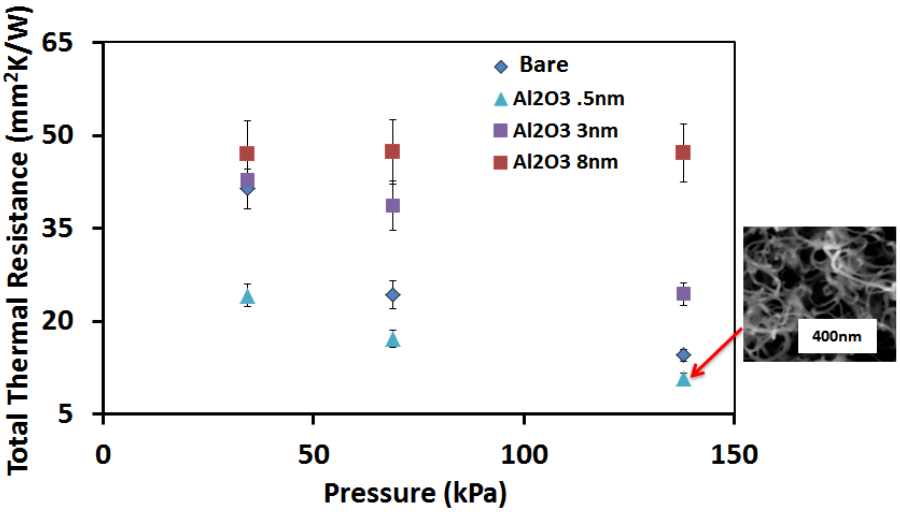

Figure 5.11 Photoacoustic total resistance measurements vs. pressure; uncertainty details may be found in Chapter 3.2.4

The most obvious trend in figure 5.9 is an increase in resistance, with an increase in Al_2O_3 coating thickness. This increase in resistance with increasing coating thickness could be justified by a model developed by Cola which correlates contact area to stiffness of the CNTs by the following equation[84]:

$$A_{r,free\ ends}/A = (2P)/B \qquad \text{Eq.5.5}$$

$A_{r,free\ ends}$ is the real contact area and A is the nominal contact between free ends of a substrate supported CNT forest and an opposing solid. P is the nominal contact pressure, and B is the effective bulk modulus of the CNT forest. Prior work shows that as Al_2O_3 coating thickness increases, the measured stiffness (uN/nm) increases.[38] If P and A are constant, then as B increases with thickness, $A_{r,free\ ends}$ must decrease. Then we look at the change in resistance from the CNT forest to the dry opposing substrate, calculated as follows[84]:

$$R''_{CNT\text{-}OS\_Actual} = (R''_{CNT\text{-}OS} * A)/ A_{r,free\ ends} \qquad \text{Eq. 5.6}$$

So as $A_{r,free\ ends}$ decreases, the resistance across the CNT metal interface increases as our measured results suggest. Another trend to note it the lower total thermal resistance of the 0.5 nm

Al_2O_3 coated forest compared to the bare forest. At low pressures contact area is extremely variable which explains why at ~38 kPa there are large differences between the 0.5 nm Al_2O_3 coated and bare forest but at ~ 140 kPa they only have a an average difference of ~3.5 mm^2K/W and a difference of ~ 2 mm^2K/W between error bars . The 2 mm^2K/W difference in total thermal resistance between the 0.5 nm Al_2O_3 coated and bare forest may be a combination of the following: the VACNT forests were grown on different days and may have a difference in effective density, the 0.5 nm coating may have a slightly larger contact area to the top substrate at the free tips effectively reducing contact resistance.

5.3 Electrical Resistance vs. Oxide Layer Thickness

Resistance measurements were taken using a 2-probe technique as described in Chapter 3.6. Two types of measurements were completed to describe electrical transport in our samples. Layer resistance is plotted to observe changes in resistivity due to oxide layer thickness, and total resistance measurements are taken to observe changes in contact resistance due to mechanical stiffness. All 2-probe measurements are reported as resistance because the exact area measured is not known due to spreading effects where current travels through the path of least resistance. Thus we perform a quantitative analysis of our system to study the path of least resistance by calculating the bulk resistance of each component in both the layer resistance measurement configuration and total resistance measurement configuration.

The layer resistance configuration shown in figure 5.12 has an individual CNT that has been coated with 15 nm of Al_2O_3, and has a CNT spacing of 30 nm (CNT spacing is 30 - 50 nm confirmed in SEM). The electrical resistivity (ρ) values used are as follows: individual MWCNT non-annealed 10 nm radius is 1.2E-6 Ω·m[92], titanium (Ti) is 420E-9 Ω·m, gold (Au) is 24.0E-9 Ω·m, aluminum (Al) is 2.8E-8 Ω·m, iron (Fe) is 1.0E-7 Ω·m, copper (Cu) is 16.8E-9 Ω·m, [93] and Al_2O_3 is 10^{14} Ω·m[94]. While the component resistances (R) were calculated as follows by eq 5.7: R_{Au} ~ 1 Ω, R_{Ti} ~ 7 Ω, $R_{Al2O3,Tip}$ ~ 3E19 Ω (15 nm coating) and ~6E18 Ω (0.5 nm coating),

R_{Al2O3} (sidewalls) ~ 5E22 Ω (15 nm coating) and ~ 5E25 Ω (0.5 nm coating), R_{CNT} ~ 1.5E5 Ω, and $R_{catalyst}$ ~ 5 Ω.

$$R=\rho*l/A \qquad \text{Eq. 5.7}$$

Where l is the characteristic length of the material, and A is the cross sectional area.

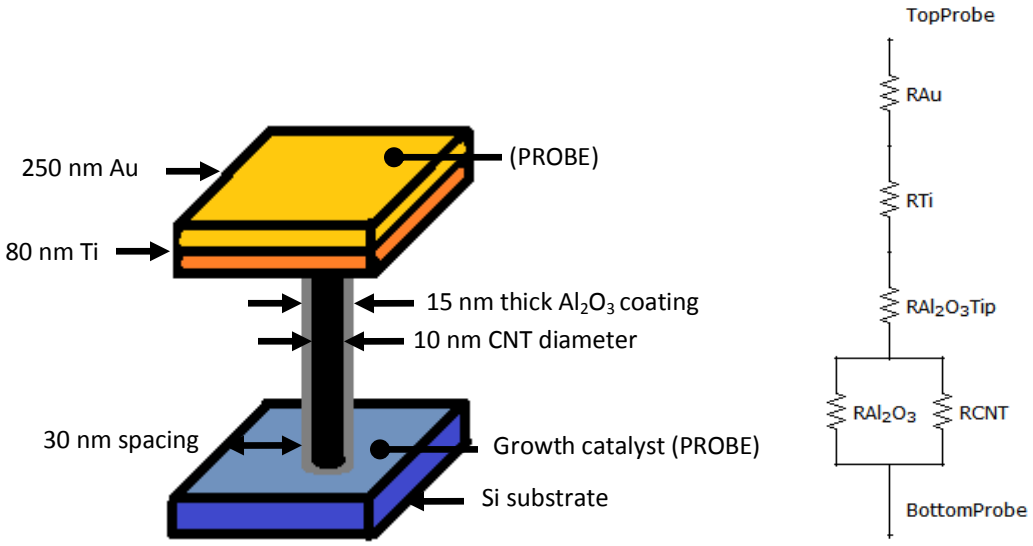

Figure 5.12 Layer electrical resistance schematic and equivalent electrical resistance circuit

The path of least resistance is through the CNTs but the current must make its way through the titatnium/gold layer from the top probe and through the growth catalyst from the bottom probe, this is where we have spreading effects. The current flows from a small area i.e probe to a much larger area i.e titanium/gold later or growth catalyst. Thus by studying the electrical resistance circuit (in figure 5.12) starting at the top probe (above the gold film layer) the current sees an additional spreading resistance when travelling through the gold/titanium layer which is much less resistant than the Al_2O_3 tip coating. Then the current travels vertically down through the Al_2O_3 coated tip (located on the free end of the CNT) which is not only a more resistant path but it also faces an additional constriction resistance (current flows from a large area to a much smaller area). On the opposite end, the bottom probe is placed on top of the growth catalyst layer (spreading) and the current must travel horizontally until it finds the least

resistant path being the CNTs adhered to the growth substrate or a more resistive path being the Al_2O_3 coating along the sidewalls of the CNTs. So the least resistant path in this case is through gold/titanium layer through the Al_2O_3 tip and into the CNTs which contains both constriction and spreading resistances. In the total resistance measurement configuration, the titanium (Ti) and Gold (Au) metal deposition film is replaced with a copper block. In this case the component resistance for the copper block is R_{Cu} ~ 2.5E-5 Ω, much less than the $R_{Al2O3,Tip}$ and again the least resistant path is through the CNTs. Consequently this analysis suggests that spreading effects do exist in both measurement techniques, so there is no effective measurement area thus values are only significant for comparing resistance values for varying oxide thickness.

The bare electrical resistance is about 30 Ω, and it appears that the 0.2 nm, 0.5 nm, 1 nm, and 3 nm Al_2O_3 coatings all slightly increase the electrical resistance to ~40 Ω at ~ 138 kPA. For Al_2O_3 coating thicknesses greater than 5nm, we see an increase in resistance with coating thickness. Because we measured across the layer of the sample, and because probe contact resistance is the same for each sample, this increase in resistance is solely attributed to the increase in Al_2O_3 thickness. For reference, the diameter of the probe ($D_{probe)}$ is 20 μm.

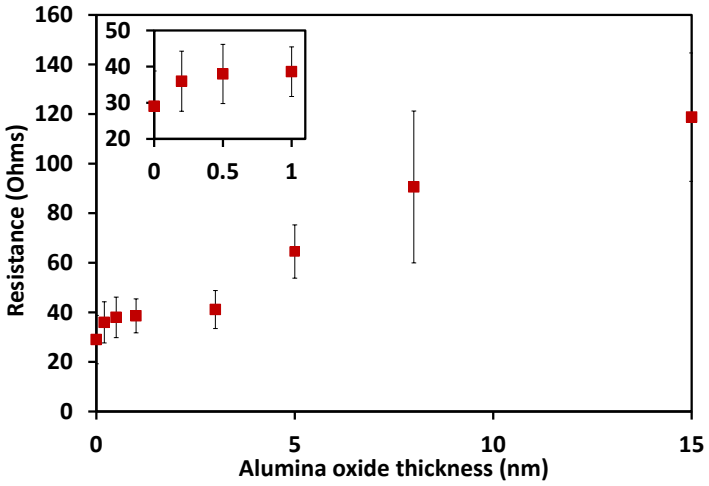

Figure 5.13 Electrical layer resistance measurements of various oxides; uncertainty details may be found in Chapter 3.2.5

Next total resistance measurements were taken with a copper block to include contact resistance at the free tips and changes in stiffness of the forest. These results were plotted in figure 5.14. The trend is very similar to the electrical layer resistance measurements. These measurements suggest that the total electrical resistance measurements are significantly greater due to contact resistance at the interface. The 15 nm thick Al_2O_3 coating is not plotted because the resistance maxed out the power supply indicating the resistance was greater than 5000 Ω. The coating thicknesses between 0.5 nm and 3 nm (inset in figure 5.14) see about a fivefold increase in electrical resistance compared to the bare forest. The total electrical resistance continues to increase drastically with increasing Al_2O_3 thicknesses greater than 3 nm because of an increase in both Al_2O_3 thickness and stiffness of the coated VACNT layer.

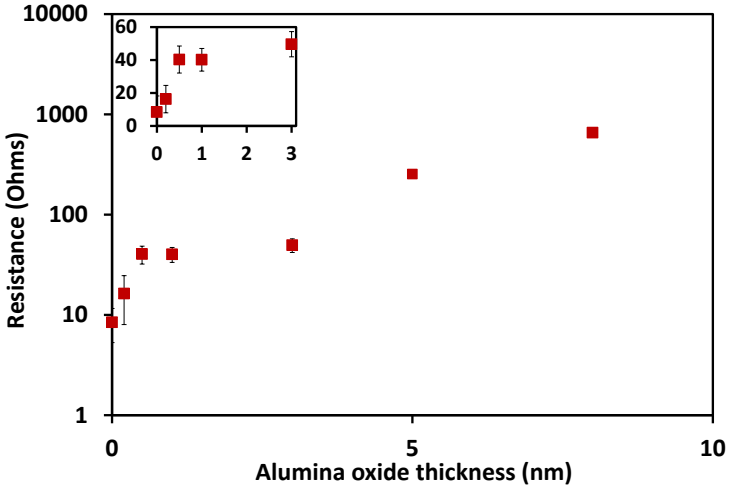

Figure 5.14 Electrical total resistance measurements of various oxides; uncertainty details may be found in Chapter 3.2.5; $A_{CopperBlockMeasured}$ = 7.9 mm^2

In order to gauge the validity of our measurements, we consider prior work where contact resistances were measured to be 20 Ω between copper-copper interfaces and 4 Ω for copper-MWCNTs (random alignment)-copper interfaces. The resistance exponentially decayed to these values upon increasing the load to ~1 N.[95] Our equivalent load is ~17 N, and our measured resistance was ~8.5 Ω which is very comparable. This difference in resistance is likely attributed

to our CNTs being vertically aligned and having a reduced effective density, which could reduce the area of contact at the surface and thus increase resistance.

6. OXIDE COATING ROBUSTNESS

In this section robustness of oxide coated VACNT forests is further investigated. The thermal stability of the oxide coated CNTs and the structural morphology (crystallinity) of the Al_2O_3 layer were studied in order to characterize the usefulness of our oxide coated VACNT forests in high power density applications and diverse environments. The structural characterization crystallinity of the Al_2O_3 layer is important for the brittleness of the material and further helps us to characterize the thermal transport in the material as discussed in Chapter 5.1.

6.1 Structural Morphology of Al_2O_3 Coating

The structural morphology (crystallinity) of the Al_2O_3 layer was studied, because it indicates the brittleness of the material and helps us better understand thermal transport in the material as discussed in Chapter 5.1. When studying the Al_2O_3 coated VACNT forests, we were unable to see sharp intense peaks for the VACNT forests; this result is in agreement with prior work that showed that the grown CNTs are well aligned.[96] For CNTs that were not well aligned, prior work has measured the following relatively weak peaks at 2θ of: (1 0 0) peak at 42.4°, (1 1 0) peak at 77.7°, and (0 0 2) peak at 26°. In our XRD measurements we see the (1 0 0) peak at 2θ in figure 6.2; this corresponds to a crystal spacing of 2.12 nm.[96] For ALD deposited Al_2O_3, prior work suggests that it is very difficult to view Al_2O_3 peaks without annealing the samples prior to measurements but the γ-Al_2O_3 (2 2 0) peak at 2θ of 33° is present in this work.[68] Al_2O_3 (1 0 0) peak at 2θ and (0 2 4) peak at 2θ were are also present and are characteristic of commercial Al_2O_3 powders and combustion synthesized Al_2O_3.[97] The intense peak we observed at 2θ = 69° (3 0 0) is a characteristic peak for Silicon substrate with a (1 0 0) orientation (See Figure 6.1), which we used as our growth substrate.[98] The XRD analysis of Al_2O_3 coatings concludes that our samples are composed of γ-Al_2O_3 coatings along the CNT sidewalls, within a forest of well aligned VACNTs.

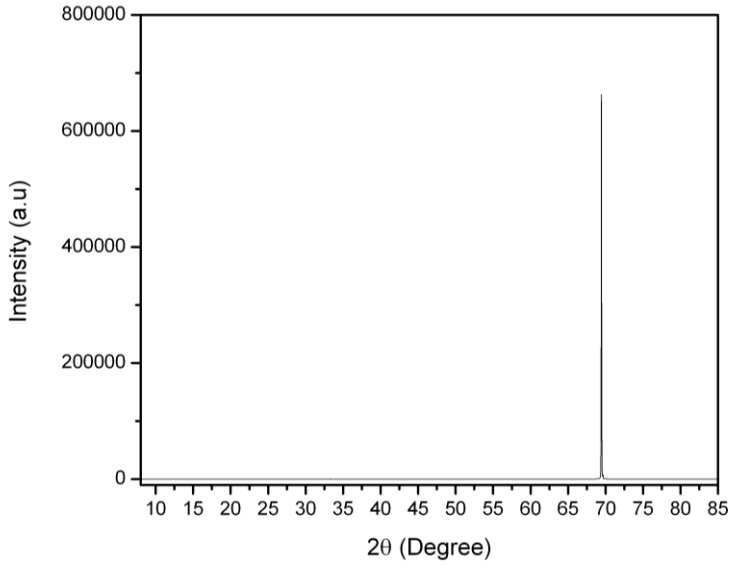

Figure 6.1 X-ray diffraction peak for 35 µm tall VACNT forest height with 8 nm of Al_2O_3 coating

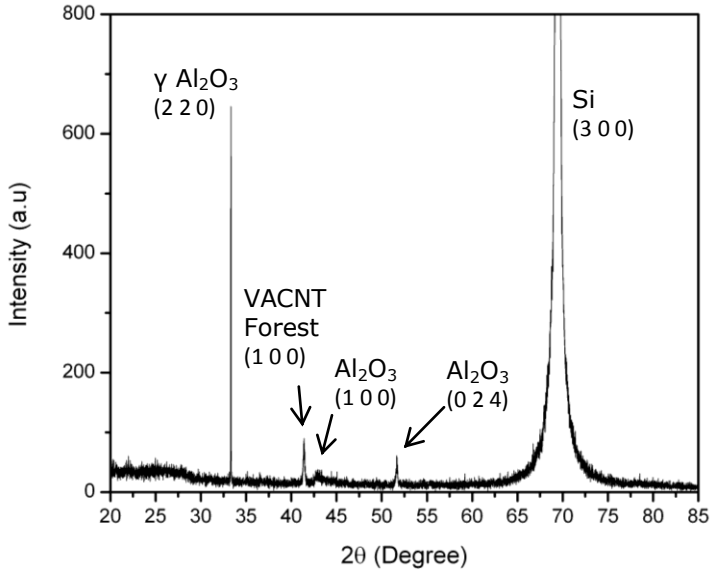

Figure 6.2 X-ray diffraction peak for 35 µm tall VACNT forest height with 8 nm of Al_2O_3 coating at lower intensities

6.2 Chemical Stability with and without Oxide Layer

The chemical inertness of the CNT graphitic structure is a major concern for high temperature applications. It also poses a major challenge for composite material fabrication. Defect sites along the walls of MWCNTs facilitate thermal oxidative destruction of the

nanotubes. To study the chemical stability at higher temperatures we thermally treated a bare, 0.5 nm thick Al_2O_3 coated, and 15 nm thick Al_2O_3 coated sample.[23] Two treatments were completed at 200 °C and 600 °C for 100 hours in air; further experimental details on thermal baking are included in are included in Chapter 3.1.3. To further estimate the thermal degradation of the CNTs, composition analysis was completed by XPS, and carbon atomic percentage pre- and post-treatment was compared. The results are summarized in table 6.1 and suggest that there was essentially no loss in carbon percentage after the 200 °C treatment. This temperature is above the operating temperature of most electronics but below the maximum temperature at which CNTs are chemically stable in air at 450 °C.[23] The increase of carbon percentage for the 15 nm coating appears to be an anomaly and is likely due to a change in ALD deposited Al_2O_3, as we had previously calculated a 9 % carbon contamination in the deposited material. Further supporting evidence that the increase in carbon percentage is an anomaly, is that even the bare forests only experienced ~1 % decrease in carbon content when treated to 200 °C, and the 0.5 nm Al_2O_3 forests saw essentially no change in carbon content after the 200 °C treatment. So we could assume that the carbon content for the 15 nm coating after the 200 °C treatment also sees no change.

Table 6.1 X-ray photoelectron spectroscopy pre and post treated data for pristine and Al_2O_3 coated VACNT forests; uncertainty details may be found in Chapter 3.2.2

Sample		*%C Pre Treatment*	*%C 200°C Treatment*	*%C 600°C Treatment*	*% Diff Pre Treatment to 600°C*
Bare		100 ± 0	99 ± 1	46 ± 1	55
Al_2O_3	**15 nm**	4 ± 1	11 ± 0	4 ± 1	6
	0.5 nm	87 ± 1	87 ± 0	15 ± 1	83

For the 600 °C treatment, however, there was a much more drastic change in carbon percentage. The bare forests had ~54 % decrease in carbon, but SEM images revealed there were no longer any standing VACNTs on the substrate as seen in Figure 6.3; this suggests that the CNTs were completely oxidized. The 0.5 nm Al_2O_3 coated forests saw ~82 % decrease in carbon, which suggests that the non-conformal Al_2O_3 coating did not protect the VACNTs and

the carbon was oxidized. Figure 6.4 shows a top view SEM image where the CNTs appear to be gone, as well as a side view where there are still tubes standing, likely due to the deposition of Al_2O_3 fully coating the outer edges of the forest. The 15 nm coating saw a slight decrease in carbon percentage of ~6 % compared to a pre-treatment measurement and a decrease of ~63 % decrease in carbon content compared to the 200 °C treated sample. Figure 6.5 shows SEM images where the coated forest appears to be unchanged. The carbon content percentage is higher in the bare forest than the Al_2O_3 coated forest because of the surface sensitivity of XPS, in the coated forests the Al_2O_3 is still left on the surface, covering any CNTs still in the sample.

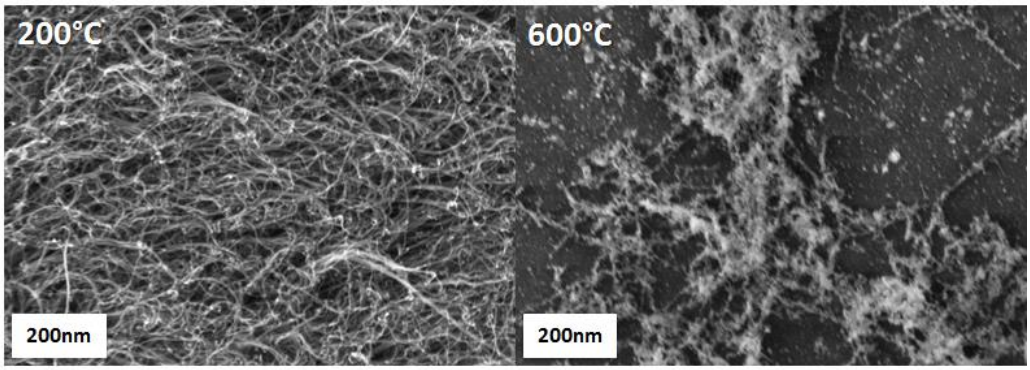

Figure 6.3 Top view SEM images of bare forest treated samples

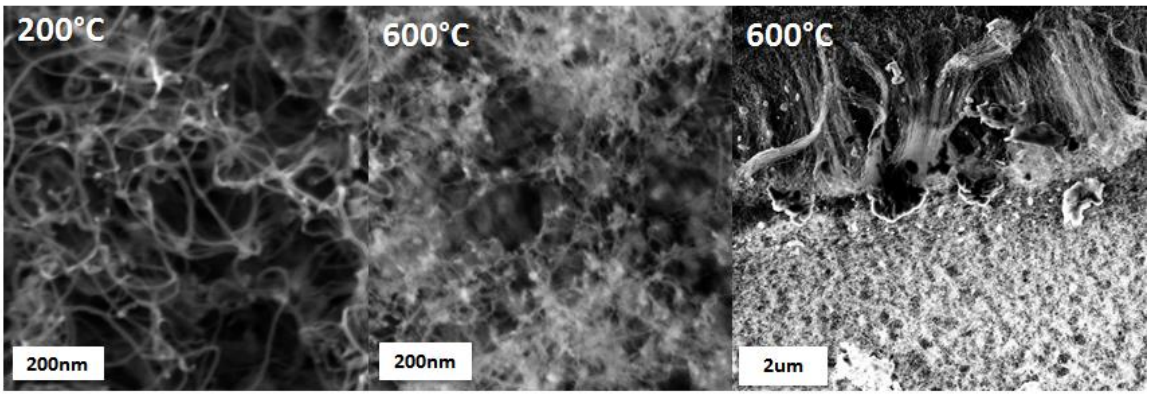

Figure 6.4 Scanning electron microscopy images of 0.5 nm Al_2O_3 coated forests treated samples (left & center) top view (right) side view

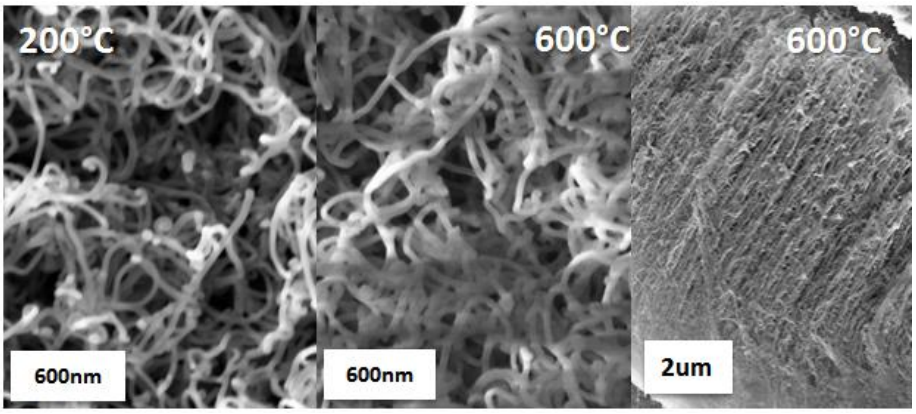

Figure 6.5 Scanning electron microscopy images of 15 nm Al_2O_3 coated forests treated samples (left & center) top view (right) side view

Thus we look at the thermal and electrical resistivity measurements to form a conclusion because the changes in carbon percentage are unclear and may not necessarily be credited to the oxidation of the carbon nanotubes. These changes in carbon percentage could be attributed to variations in ALD deposition due to its carbon contamination that was observed when deposited as a thin film (discussed in Chapter 4.3), or to variation in XPS spectra measurements due to its high surface sensitivity.

Thermal resistance measurements were performed to study the effect of thermal treatment on thermal transport. Figure 6.6, shows that the bare forest measurements remained about the same pre and post treatment at 200 °C but after the 600 °C treatment, a drastic increase was observed. This is expected since the VACNTs were essentially oxidized and a measured increase in thermal resistance is due to dry contact between the silver foil and oxidized CNTs on a silicon substrate. The trend of decreasing resistance with increasing pressure seen in figure 6.6, is attributed to the CNTs being mechanically compliant and having an increase in contact area with increasing pressure (as discussed in Chapter 5.2) which decreases the resistance. At low pressures below ~ 70 kPa, the variability in contact area is large (also discussed in Chapter 5.2). This explains why the pre-treatment forest and 200 °C treated forest have large differences in resistance at these lower pressures (< 70 kPa), but at higher pressures of ~ 138 kPa they have essentially the same resistance.

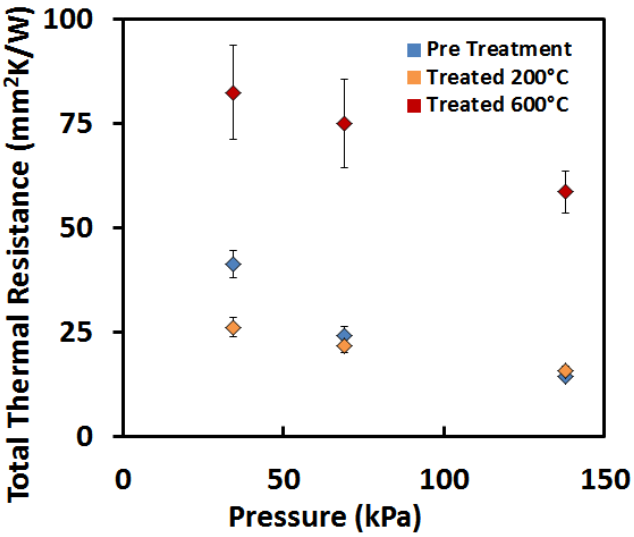

Figure 6.6 Bare VACNT forests PA total resistance measurements through thermal treatments; uncertainty details may be found in Chapter 3.2.4

The 0.5 nm Al_2O_3 coated forests, shown in figure 6.7, saw a slight decrease in resistance from the pre-treated forests to the forests treated to 200 °C (note that the error bars for the pre-treatment and 200 °C treated forests are small relative to the length scale of the plot and consequently are not visible). Considering the pre-treatment 0.5 nm coated forests saw a decrease in resistance with pressure (also shown in figure 5.11), and that the 0.5 nm Al_2O_3 coated thermally treated forests didn't have much of a trend with pressure, suggests the CNTs were no longer 'soft' or mechanically compliant after thermal treatment. Thus we may conclude that this increase in stiffness may be the reason for the slight increase in thermal resistance from the pre-treated to 200 °C treated forests. After the 600 °C treatment a drastic increase in resistance was observed which may be attributed to the oxidation of CNTs, which effectively increases the resistance of the layer.

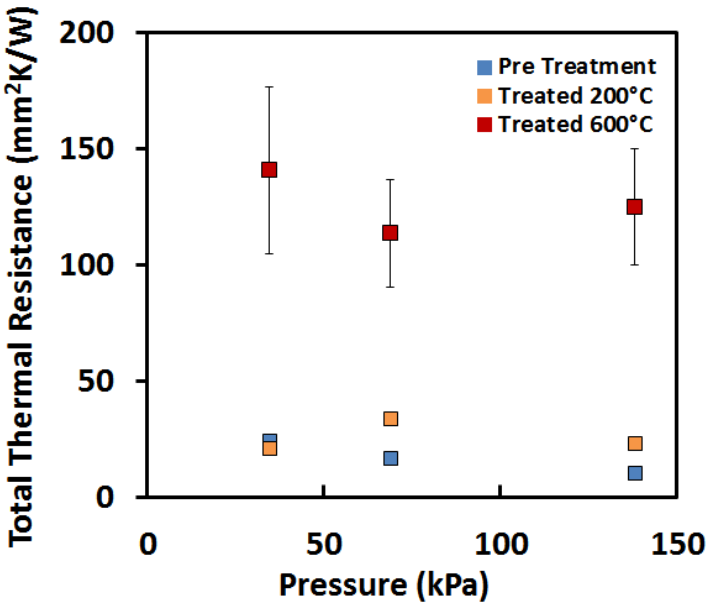

Figure 6.7 VACNT forests with 0.5 nm Al_2O_3 coating PA total resistance measurements through thermal treatments; uncertainty is plotted but not visible for the pre-treated and 200°C treated samples because the y-axis scaling is larger and they are smaller than the data points (further uncertainty details may be found in Chapter 3.2.4)

For the 15 nm Al_2O_3 coated forests (shown in figure 6.8), the pre-treatment and 200 °C treatment produce essentially the same resistances considering the variability of contact area at low pressures (< 70 kPa). However, the 600 °C treatment has a drastic increase in resistance. This increase in resistance is likely due to the oxidation of CNTs, which effectively increases the resistance of the layer. The pre-treated and 200 °C treated forests show little to no trend of increasing resistance with pressure but the 600 °C treated forests shows a clear trend of increasing resistance with pressure. We know from Chapter 5.2 that the 15nm coating is mechanically stiff and we showed in figure 6.7, that the CNTs are likely becoming more stiff after thermal treatment which suggests the resistance measurements should not change with pressure. Considering the large error bars for the 600 °C treatment, the increasing resistance trend could be a result of variability in contact area at low pressures, especially considering the pre-treated and 200 °C treated forest produce essentially the same resistances at ~ 70 kPa and ~140 kPa.

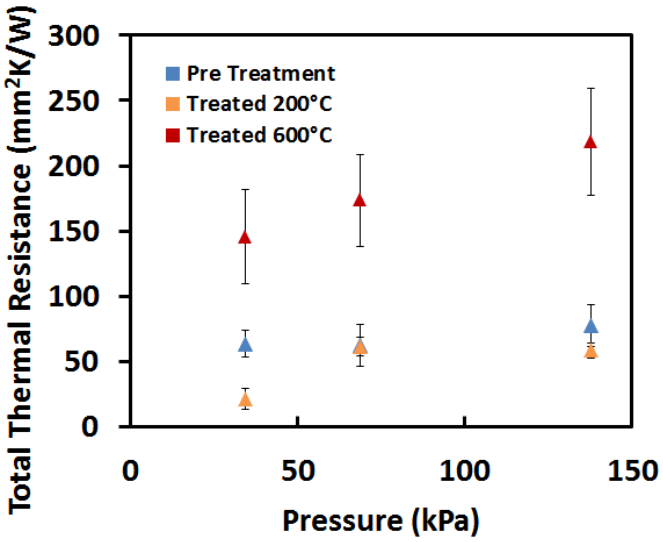

Figure 6.8 VACNT forests with 15 nm Al_2O_3 coating PA total resistance measurements through thermal treatments; uncertainty details may be found in Chapter 3.2.4

Table 6.2 summarizes the electrical layer resistances of pre-treated and treated samples. From the non-treated to the samples treated up to 200 °C, the bare sample and 0.5 nm coatings see a 20-28 % increase in resistance (as seen in figure 6.9) , which is likely attributed to the small loss of CNTs. The 15nm coated samples sees almost a two fold increase in resistance, which may be attributed to a larger loss in carbon nanotubes or a change in Al_2O_3 morphology. When treated to 600 °C, the bare sample resistance increases from ~30 Ω to ~180 Ω, while the 0.5 nm and 15 nm coatings max out the power supply, suggesting a resistance > 5000 Ω. This difference in resistances from the bare to the coated forests is expected because the bare forest does not have Al_2O_3 which has a high electrical resistivity. Although the bare forest does have a catalyst layer whose iron layer likely oxidized which is contributing to this electrical resistance on the bare forest.[99] The coated samples have left Al_2O_3 on the surface of the substrate causing a drastic increase in resistance. Thus we may conclude that the conformal coatings did not help to stabilize the VACNT forests up to 600 °C as predicted, but the Al_2O_3 coated forests are stable up to 200 °C in air. Upon treating to 200 °C in air, not only did the coated forests perform equally as well in thermal resistance measurements, but they actually become further electrically insulated.

Table 6.2 Electrical layer resistance measurements of thermal treated samples, measurements > 5000 Ω exceeded the systems limit; uncertainty details may be found in Chapter 3.2.5

Sample	Non Treated (Ω)	Treated 200°C (Ω)	Treated 600°C (Ω)
Bare VACNT	29.02 ± 9.76	35.14 ± 7.00	182.94 ± 37.33
Al_2O_3 0.5nm	37.98 ± 8.18	49.34 ± 40.95	> 5000
Al_2O_3 15nm	118.75 ± 25.88	201.0 ± 47.37	> 5000

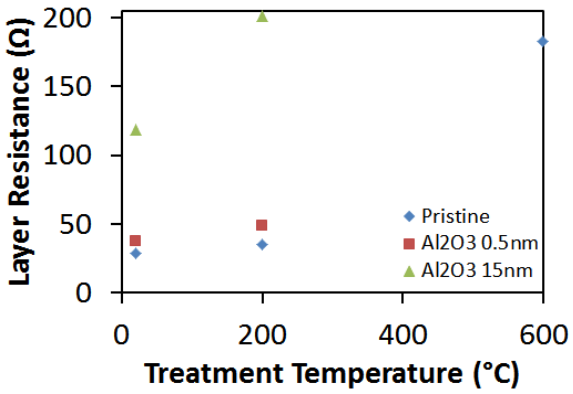

Figure 6.9 Electrical layer resistance for thermal treated samples; uncertainty details may be found in Chapter 3.2.5

7. CONCLUSIONS

This thesis has demonstrated several of the important factors that need to be considered when fabricating oxide coated VACNT forests. Uniformly thick conformal coatings were achieved for the first time by functionalizing the VACNT forests with O_2 plasma pretreatment prior to oxide ALD. A complete chemical characterization was completed which allowed us to conclude that we had conformal amorphous Al_2O_3 coatings for thicknesses greater than 3 nm. Thermal and electrical performance was also evaluated by measuring total resistance values. Figure 7.1 plots both thermal and electrical resistance for measurements taken at ~ 138 kPa. Because TIMs are typically bonded as a die attach material at much greater pressures, this gives us the best comparison for total resistance values. Coating thicknesses from 0.5 nm to 3 nm give us the best thermal conductance for electrical insulation. As we increased oxide thickness, further increasing electrical insulation, thermal conductance is compromised. We also determined that coating thicknesses less than or equal to ≤ 3 nm are still mechanically compliant, and as coating thicknesses increase > 3 nm the forests become more stiff, increasing contact resistance and brittleness. If we take our conformally coated 3 nm thick Al_2O_3 forest, we would have a total thermal resistance value of ~25 mm^2K/W, and a total electrical resistance value of ~50 Ω that is chemically stable up to 200 °C in air.

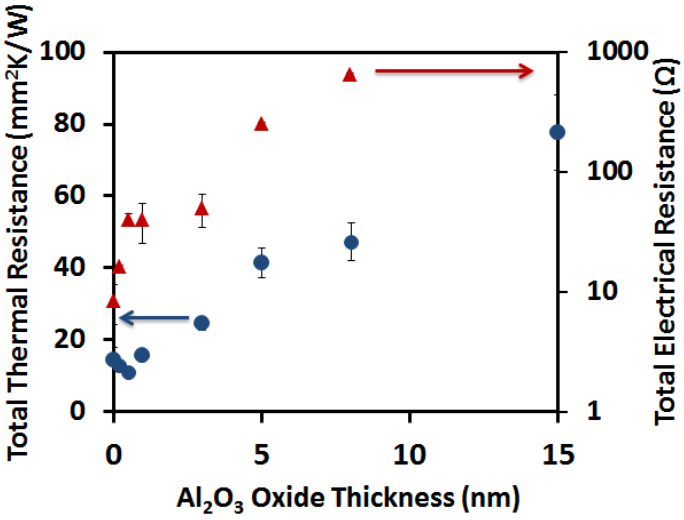

Figure 7.1 Total thermal resistance and total electrical resistance vs. Al_2O_3 thickness at ~ 138 kPa; uncertainty details may be found in Chapter 3.2.4 and Chapter 3.2.5

The following bullets summarize key findings in this work and are presented to facilitate the fabrication of oxide coated VACNT forests with enhanced thermal conductance and electrical insulation properties:

- O_2 plasma pretreatment of the VACNT forests had no significant effect on CNT quality. Because the diffusive process is extremely slow in solids, it is likely that only the outer shell of the MWCNTs is functionalized.

- The Al_2O_3 coatings were conformal for thicknesses greater than 1nm, confirmed through SEM and TEM images. Contact angle measurements also confirmed this conclusion because the samples became hydrophilic at thicknesses > 1nm, thus confirming the absence of VdW forces between CNT sidewalls.

- The AlN, ZnO and Pt oxide coatings were not conformal when deposited with 30 second exposure times; this is longer than the suggested exposure time of 3 seconds.

- The effective thermal conductivity measurements were constant across varying Al_2O_3 coating thicknesses and bare forests. This was justified by a parallel thermal resistance

model, as well as by Goyny's study, which suggests the shielded internal layers of a MWCNT promote the conduction of phonons and minimize coupling losses.

- The effective density of the VACNT layer plays a large role on the calculated effective thermal diffusivity and heat capacity, but it was not sensitive in the PA fitted thermal conductivity values. This suggests that our effective density is significantly lower than the measured bulk value of ~ 310 kg/m^3.

- Al_2O_3 coating thicknesses less than or equal to 3 nm produce forests that are still mechanically compliant, thus increasing effective contact area, decreasing contact resistance, and increasing energy transport across the interface.

- Total electrical resistance increases 5 fold for Al_2O_3 thicknesses of 0.2 nm to 3 nm compared to bare forests. Coating thicknesses greater than 3nm have a linear increase in electrical resistance with increasing thickness, which was attributed to both an increase in in Al_2O_3 thickness, and an increase in contact resistance due to increased stiffness of the forests.

- A thermal treatment analysis showed that our coatings are chemically stable in air up to 200 °C. Upon treating to 200 °C in air, not only did the coated forests perform equally well in thermal resistance measurements but they actually become further electrically insulated.

- Amorphous Al_2O_3 coatings were achieved and considering they had no effect on the effective thermal conductivity, a crystal Al_2O_3 structure would only increase stiffness of the tubes.

As a baseline comparison, the Bergquist Company developed electrically insulating and thermally conductive TIMs with thermal layer resistances > 280 mm^{2}K/W, and volume resistance = 10^{11} Ω·m, stable up to 180°C. Our samples already perform much better thermally

but the electrical insulation still needs further improvement. This is addressed at the end of section 7.1.

7.1 Recommendations

Beginning with ALD deposition of oxide metals; figure 7.2 indicates that ZnO and Pt produce smaller thermal resistances at higher pressures than Al_2O_3 does. Thus modifying these two recipes to achieve conformal coatings may prove to be beneficial. Pt and ZnO use different precursors, and because Zn and Pt have much heavier atomic masses than Al, the exposure and purge times may need to be longer than the 30 seconds allotted, to allow these heavier materials to settle on the surface of the CNT sidewalls. For Al_2O_3, ZnO, and Pt, the ALD recipes could be further fine-tuned to achieve conformal coatings at thinner oxide layers by:

- Using a direct plasma treatment instead of a remote plasma treatment which may have an extinction of radicals as they diffuse into the forest which may be preventing functionalization of the CNTs away from the tip region.

- Depositing at higher temperatures, increasing kinetic energy so that the precursor material could reach the CNTs more efficiently.

- Optimizing precursor exposure and purge times to allow the precursor material to settle to the surface of the CNTs and form conformal coatings; extending exposure times infinitely may ideally allow for conformal uniform coatings but the processing time is limited by production time.

- Using O_2 plasma treatment in between the first few ALD cycles to further increase nucleation sites along the exposed CNT sidewall locations that have not yet been coated by oxide metal.

- Using O_2 plasma ALD deposition instead of thermal, since it has proven to produce higher dielectric constants for the deposited Al_2O_3, and has excellent conformity for films deposited on macropores.[100]

- Depositing an Al_2O_3 seed layer to form conformal coatings of other coatings.[101]

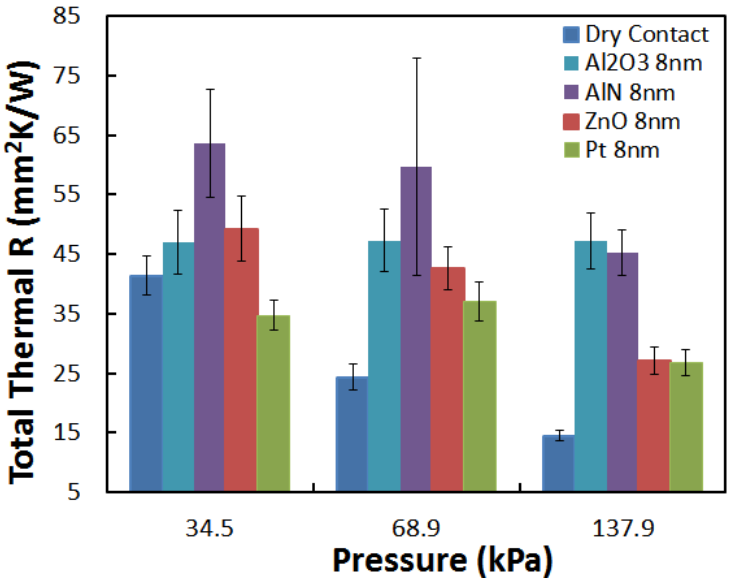

Figure 7.2 Various oxide total thermal resistance vs. pressure; uncertainty details may be found in Chapter 3.2.4

Several studies in literature have shown that rapid thermal annealing of CNTs in inert atmosphere vacuum such as N_2 up to temperatures of about 2800 °C reduces impurities in the CNT structure. These reductions in impurities were observed by Raman spectroscopy where the D-band peak intensity decreased and the G-band peak intensity remained constant.[52] Although we need defect sites prior to ALD to achieve conformal coatings, post processing techniques are compromised by defect sites. Annealing has been shown to take MWCNTs from being chemically stable in air up to ~450 °C to ~650 °C.[23] Annealing has also been shown to lead to ohmic contact of a VACNT/metal interface, as well as to increase XRD peak intensity.[61, 96] Hence rapid thermal annealing could potentially prove useful for the oxide coated VACNT forests even after ALD deposition, to see if it has any effect on CNT quality and stability then. Thermogravimetric analysis would also be useful in the future to look at changes in mass of

carbon and to study the physical and chemical properties of the oxide coating as a function of temperature.[23] Another worthwhile pursuit includes growing more dense VACNT forests with larger diameter CNTs to further reduce thermal resistance by increasing effective density and contact area. Prior work shows that controlling the timing and duration of hydrogen exposure in a thermal growth process allows for control of these parameters.[102]

Because the main concern in this work is still the low electrical resistance compared to that of existing commercial materials, current work is ongoing to bond the oxide coated VACNT forests with a top metal foil using organic polymer linkers. Polymer linkers have been shown to reduce contact resistances by 85 %[103], and if electrically insulating polymers are used, it is possible to further reduce electrical conductance across the interface.

A. Appendix A: X-ray Photoelectron Spectrocopy Data

Table A.1 X-ray photoelectron spectroscopy for the various oxide metal coatings on VACNT forests

Sample		%C	%O	%Al	%N
Pristine		100	0	0	0
AlN	8nm	38.19 ± 0.98	30.56 ± 0.49	20.68 ± 0.35	10.64 ± 0.20
Al2O3	8nm	6.58 ± 0.36	54.23 ± 2.17	39.22 ± 1.78	
		%C	%O	%Zn	
ZnO	8nm	9.68 ± 0.51	48.09 ± 0.48	42.22 ± 0.43	
		%C	%O	%Pt	
Pt	8nm	26.92 ± 1.31	11.95 ± 2.79	61.13 ± 1.50	

Table A.2 X-ray photoelectron spectroscopy for the various O_2 plasma pretreatments on VACNT forests

Sample		%C	%O
Pristine		100	0
O2	1m,300W, 20sccm	97.72 ±0.09	2.27 ±0.09
	3m,300W, 20sccm	97.14 ±0.07	2.86 ±0.07
	5m,300W, 20sccm	97.14 ±0.21	2.86 ±0.21
O2	1m, 300W, 100sccm	95.42 ±0.29	4.58 ±0.29
	3m, 300W, 100sccm	93.42 ±0.76	6.58 ±0.76
	5m, 300W, 100sccm	92.57 ±0.07	7.43 ±0.07
O2	1m, 100W, 20sccm	100	0
	3m, 100W, 20sccm	95.05 ±0.10	4.95 ±0.10
	5m, 100W, 20sccm	94.50 ±0.05	5.50 ±0.05

REFERENCES

[1] (2007, The Basics of Package/Device Cooling. Available: http://www.thomasnet.com/white-papers/abstract/100775/the-basics-of-package-device-cooling.html#null

[2] D. L. Tapellini, "Our test finds new iPad hits 116 degrees while running games," in *Consumer Reports*, ed. ConsumerReports.org, 2012.

[3] R. Bornoff. (2010, Identifying Thermal Bottlenecks and Shortcut Opportunities - Taking Simulation to the Next Level. Available: http://www.electronics-cooling.com/2010/10/identifying-thermal-bottlenecks-and-shortcut-opportunities-taking-simulation-to-the-next-level/

[4] S. Kang, "Advanced cooling for power electronics," *Integrated Power Electronics Systems (CIPS)*, 2012.

[5] (2013). *Thermal Management for LEDs and Power Electronics Expected to More Than Double*. Available: http://www.solarnovus.com/thermal-management-for-leds-and-power-electronics-expected-to-more-than-double_N7101.html

[6] D. D. L. Chung, "Carbon materials for structural self-sensing, electromagnetic shielding and thermal interfacing," *Carbon*, vol. 50, 2012.

[7] "Haitz's law," *Nature Photonics*, vol. 1, 2007.

[8] T. B. Company. (2014, April 10, 2014). *LEDs - TIM Solutions*. Available: www.bergquistcompany.com/thermal_substrates/LEDs/timSolutions.html

[9] J. Coupal, "IGBT Thermal Management," in *CPS Technologies Blog* vol. 2014, ed. CPS Technologies, 2011.

[10] F. Miyashiro, N. Iwase, A. Tsuge, and F. Ueno…, "High thermal conductivity aluminum nitride ceramic substrates and packages," *Components*, 1990.

[11] Y. Guo, C. K. Lim, W. T. Chen, and C. G. Woychik, "Solder Ball Connect (SBC) assemblies under thermal loading: I. Deformation measurement via moiré interferometry, and its interpretation," *IBM Journal of Research and Development*, vol. 37, 1993.

[12] R. Prasher, "Thermal Interface Materials: Historical Perspective, Status, and Future Directions," *Proceedings of the IEEE*, vol. 94, 2006.

[13] F. Sarvar, D. C. Whalley, and P. P. Conway, "Thermal interface materials-A review of the state of the art," *IEEE*, vol. 2, pp. 1292-1302, 2006.

[14] (2014). *Nanothermal Interfaces (NTI)*. Available: http://www.darpa.mil/Our_Work/MTO/Programs/TMT/NanoThermal_Interfaces_(NTI).aspx

[15] L. Liyanage, D. Cott, and A. Delabie…, "Atomic layer deposition of high-k dielectrics on single-walled carbon nanotubes: a Raman study," *...*, 2013.

[16] P. R. Bandaru, "Electrical properties and applications of carbon nanotube structures," *Journal of nanoscience and nanotechnology*, vol. 7, pp. 4-5, 2007.

[17] A. M. Marconnet, Panzer, M. A., & Goodson, K. E. , "Thermal Conduction Phenomena in Carbon Nanotubes and Related Nanostructured Materials," *Reviews of Modern Physics*, vol. 85(3), 2012.

[18] M. De Volder, S. Tawfick, R. Baughman, and A. Hart, "Carbon nanotubes: present and future commercial applications," *Science (New York, N.Y.)*, vol. 339, pp. 535-539, 2013.

[19] C. Muhich, B. Evanko, K. Weston, P. Lichty, and X. Liang…, "Efficient Generation of H2 by Splitting Water with an Isothermal Redox Cycle," *Science,* 2013.
[20] K. Ahmad, W. Pan, and S. Shi, "Electrical conductivity and dielectric properties of multiwalled carbon nanotube and alumina composites," *Applied physics letters,* 2006.
[21] M. Terrones, "Science and technology of the twenty-first century: synthesis, properties, and applications of carbon nanotubes," *Annual review of materials research,* vol. 33, pp. 419-501, 2003.
[22] M. Falvo, G. Clary, R. Taylor, V. Chi, and F. Brooks…, "Bending and buckling of carbon nanotubes under large strain," *Nature,* 1997.
[23] D. Bom, R. Andrews, D. Jacques, J. Anthony, and B. Chen…, "Thermogravimetric analysis of the oxidation of multiwalled carbon nanotubes: evidence for the role of defect sites in carbon nanotube chemistry," *Nano Letters,* 2002.
[24] H. Tobias, M. Richard, and A. Phaedon, "Manipulation of Individual Carbon Nanotubes and Their Interaction with Surfaces," *The Journal of Physical Chemistry B,* vol. 102, 1998.
[25] C. McCarter, R. Richards, and S. Mesarovic…, "Mechanical compliance of photolithographically defined vertically aligned carbon nanotube turf," *Journal of materials …,* 2006.
[26] P. Abadi, "Effects of morphology on the micro-compression response of carbon nanotube forests," *Nanoscale,* 2012.
[27] Y. Gao, A. Marconnet, R. Xiang, and S. Maruyama…, "Heat Capacity, Thermal Conductivity, and Interface Resistance Extraction for Single-Walled Carbon Nanotube Films Using Frequency-Domain Thermoreflectance," 2013.
[28] P. F. D. L. Schodek, M. F. Ashby, , *Nanomaterials, Nanotechnologies and Design: An Introduction for Engineers and Architects*: Butterworth-Heinemann, 2009.
[29] D. Geohegan, A. Puretzky, and I. Ivanov…, "In situ growth rate measurements and length control during chemical vapor deposition of vertically aligned multiwall carbon nanotubes," *Applied physics …,* 2003.
[30] O. Hildreth, B. Cola, and S. Graham…, "Conformally coating vertically aligned carbon nanotube arrays using thermal decomposition of iron pentacarbonyl," *Journal of Vacuum …,* 2012.
[31] S. George, "Atomic layer deposition: an overview," *Chemical reviews,* vol. 110, pp. 111-131, 2010.
[32] M. Panzer, H. Duong, J. Okawa, J. Shiomi, B. Wardle, S. Maruyama, *et al.*, "Temperature-dependent phonon conduction and nanotube engagement in metalized single wall carbon nanotube films," *Nano letters,* vol. 10, pp. 2395-2400, 2010.
[33] Y. Zhang, Q. Zhang, Y. Li, N. Wang, and J. Zhu, "Coating of carbon nanotubes with tungsten by physical vapor deposition," *Solid state communications,* 2000.
[34] Y. Zhang, W. F. Nathan, J. C. Robert, and D. Hongjie, "Metal coating on suspended carbon nanotubes and its implication to metal–tube interaction," *Chemical Physics Letters,* vol. 331, 2000.
[35] M.-G. Willinger, G. Neri, A. Bonavita, G. Micali, E. Rauwel, T. Herntrich, *et al.*, "The controlled deposition of metal oxides onto carbon nanotubes by atomic layer deposition: examples and a case study on the application of V2O4 coated nanotubes in gas sensing," *Physical chemistry chemical physics : PCCP,* vol. 11, pp. 3615-3622, 2009.

[36] J. S. Lee, B. Min, K. Cho, S. Kim, J. Park, Y. T. Lee, *et al.*, "Al2O3 nanotubes and nanorods fabricated by coating and filling of carbon nanotubes with atomic-layer deposition," *Journal of Crystal Growth,* vol. 254, 2003.
[37] C. Herrmann, F. Fabreguette, D. Finch, R. Geiss, and S. George, "Multilayer and functional coatings on carbon nanotubes using atomic layer deposition," *Applied Physics Letters,* vol. 87, p. 123110, 2005.
[38] P. Abadi, M. Maschmann, and J. Baur…, "Deformation response of conformally coated carbon nanotube forests," *...,* 2013.
[39] H. Dai, "Carbon nanotubes: synthesis, integration, and properties," *Accounts of chemical research,* vol. 35, pp. 1035-1044, 2002.
[40] S. Sinnott, R. Andrews, D. Qian, A. Rao, and Z. Mao…, "Model of carbon nanotube growth through chemical vapor deposition," *Chemical Physics ...,* 1999.
[41] M. Arnaud, S. Jin Won, S. Rita, M. Marijana, and F. László, "Catalytic CVD Synthesis of Carbon Nanotubes: Towards High Yield and Low Temperature Growth," *Materials,* vol. 3, 2010.
[42] B. R, "Formation of filamentous carbon from iron, cobalt and chromium catalyzed decomposition of acetylene," *Journal of Catalysis,* vol. 30, 1973.
[43] H. Zhidong and F. Alberto, "Thermal conductivity of carbon nanotubes and their polymer nanocomposites: A review," *Progress in Polymer Science,* vol. 36, 2011.
[44] B. Lee, S.-Y. Park, H.-C. Kim, K. Cho, E. M. Vogel, M. J. Kim, *et al.*, "Conformal Al2O3 dielectric layer deposited by atomic layer deposition for graphene-based nanoelectronics," *Applied Physics Letters,* vol. 92, p. 203102, 2008.
[45] J. W. Elam, J. A. Libera, M. J. Pellin, and P. C. Stair, "Spatially controlled atomic layer deposition in porous materials," *Applied Physics Letters,* vol. 91, 2007.
[46] L. Markku, K. Marianna, K. Kaupo, P. Viljami, S. Eero, R. Mikko, *et al.*, "Exploitation of atomic layer deposition for nanostructured materials," *Materials Science and Engineering: C,* vol. 27, 2007.
[47] Ultratech/CambridgeNanotech. (2011, Atomic Layer Deposition Tutorial. Available: http://www.cambridgenanotechald.com/atomic-layer-deposition-tutorial.shtml
[48] W. Li, H. Zhang, C. Wang, Y. Zhang, and L. Xu…, "Raman characterization of aligned carbon nanotubes produced by thermal decomposition of hydrocarbon vapor," *Applied Physics ...,* 1997.
[49] Y. Ouyang and Y. Fang, "Temperature dependence of the raman spectra of carbon nanotubes with 1064nm excitation," *Physica E: Low-dimensional Systems and ...,* 2004.
[50] Characterization of Carbon Nanotubes (CNTs) with Raman Spectroscopy. Available: https://www.youngin.com/application/CNT.pdf
[51] M. Dresselhaus, G. Dresselhaus, R. Saito, and A. Jorio, "Raman spectroscopy of carbon nanotubes," *Physics Reports,* 2005.
[52] N. Tam, Nghia,N., Quynh,N., Khoi,P., Minh, P. , "Analyzing the Purity of Carbon Nanotubes by Using Different Methods," *Journal of the Korean Physical Society,* vol. 52, pp. 1382-1385, 2008.
[53] T. P. K. Laboratory. (2012). *Raman Spectroscopy*. Available: http://www3.nd.edu/~kamatlab/facilities_spectroscopy.html#Pos7
[54] C. Bonnelle, ". X-Ray spectroscopy," *Annual Reports Section" C"(Physical Chemistry),* vol. 84, pp. 201-272, 1987.

[55] H. P. Klug and L. E. Alexander, "X-ray diffraction procedures: for polycrystalline and amorphous materials," *X-Ray Diffraction Procedures: For Polycrystalline and Amorphous Materials, 2nd Edition, by Harold P. Klug, Leroy E. Alexander, pp. 992. ISBN 0-471-49369-4. Wiley-VCH, May 1974.*, vol. 1, 1974.
[56] X. Wang, B. Cola, and T. Bougher…, "Photoacoustic technique for thermal conductivity and thermal interface measurements," *Annual Review of ...,* 2013.
[57] H. Hu, X. Wang, and X. Xu, "Generalized theory of the photoacoustic effect in a multilayer material," *Journal of applied physics,* 1999.
[58] A. C. Baratunde, X. Jun, C. Changrui, X. Xianfan, S. F. Timothy, and H. Hanping, "Photoacoustic characterization of carbon nanotube array thermal interfaces," *Journal of Applied Physics,* vol. 101, 2007.
[59] C. V. T. Bougher, and B. Cola, "Thermal Conductivity Measurement of Bare Carbon Nanotube Films using the Photoacoustic Technique," in *15th International Heat Transfer Conference*, Kyoto, Japan, 2014.
[60] S. Masahito, Y. Kashiwagi, Y. Li, and K. Arstila…, "Measuring the electrical resistivity and contact resistance of vertical carbon nanotube bundles for application as interconnects," *...,* 2011.
[61] W. Choi, E. Bae, D. Kang, S. Chae, and B. Cheong…, "Aligned carbon nanotubes for nanoelectronics," *...,* 2004.
[62] C. Liu and S. Fan, "Effects of chemical modifications on the thermal conductivity of carbon nanotube composites," *Applied Physics Letters,* 2005.
[63] K. Stano, R. Chapla, M. Carroll, and J. Nowak…, "Copper-Encapsulated Vertically Aligned Carbon Nanotube Arrays," *... applied materials & ...,* 2013.
[64] E. L. Cussler, *Diffusion: mass transfer in fluid systems*: Cambridge University Press, 2009.
[65] W. D. Callister, & Rethwisch, D. G. , *Fundamentals of materials science and engineering: an integrated approach*: John Wiley & Sons., 2012.
[66] J. A. D. a. N. A. Lange, *Lange's handbook of chemistry*: McGraw-Hill: New York. p. v., 1973.
[67] L. Anderson Oliveira, R. Sandra Cristina, A. Erica Freire, M. Fernanda Roberta, T.-A. Vladimir Jesus, and C. Evaldo Jose, "Fast functionalization of vertically aligned multiwalled carbon nanotubes using oxygen plasma," *Materials Letters,* vol. 70, 2012.
[68] S. Yun, Kang,J., Paek,M., Nam,K., " Large-Area Atomic Layer Deposition and Characterization of Al_2O_3 Film Grown Using AlCl3 and H2O," *Journal of the Korean Physical Society,* vol. 33, pp. S170-S174, 1998.
[69] C. Bonnelle, *Advances in X-ray spectroscopy*: Pergamon Press, 1982.
[70] *Handbook of Monochromatic XPS Spectra; Vol. 2 Commercially Pure Binary Oxides* XPS International, Inc., 1999.
[71] A. Cappella, J. Battaglia, and V. Schick…, "High Temperature Thermal Conductivity of Amorphous Al2O3 Thin Films Grown by Low Temperature ALD," *Advanced ...,* 2013.
[72] J. Yang, Y. Yang, S. Waltermire, T. Gutu, A. Zinn, and T. Xu…, "Measurement of the intrinsic thermal conductivity of a multiwalled carbon nanotube and its contact thermal resistance with the substrate," *Small,* 2011.
[73] P. Kim, Shi, L., Majumdar, A., & McEuen, P. L., "Thermal transport measurements of individual multiwalled nanotubes," in *Physical review letters* vol. 87 (21), ed, 2001.
[74] W. Press, "Numerical recipes 3rd edition: The art of scientific computing," 2007.

[75] C. Masarapu, L. Henry, and B. Wei, "Specific heat of aligned multiwalled carbon nanotubes," *Nanotechnology,* 2005.
[76] Z. Yang, L. Ci, J. Bur, S. Lin, and P. Ajayan, "Experimental observation of an extremely dark material made by a low-density nanotube array," *Nano letters,* 2008.
[77] H. Ye, X. Wang, W. Lin, and C. Wong…, "Infrared absorption coefficients of vertically aligned carbon nanotube films," *Applied Physics ...,* 2012.
[78] X. Hu, E. Pop, and H. Dai…, "Thermal properties of metal-coated vertically aligned single-wall nanotube arrays," *Journal of ...,* 2008.
[79] H. Sugime, S. Esconjauregui, and J. Yang…, "Low temperature growth of ultra-high mass density carbon nanotube forests on conductive supports," *Applied Physics ...,* 2013.
[80] Y. Gao, A. Marconnet, M. Panzer, and S. LeBlanc…, "Nanostructured interfaces for thermoelectrics," *Journal of Electronic ...,* 2010.
[81] M. Bedewy and A. Hart, "Mechanical coupling limits the density and quality of self-organized carbon nanotube growth," *Nanoscale,* 2013.
[82] H. G. Florian, H. G. W. Malte, F. Bodo, A. K. Ian, B. Wolfgang, H. W. Alan, *et al.*, "Evaluation and identification of electrical and thermal conduction mechanisms in carbon nanotube/epoxy composites," *Polymer,* vol. 47, 2006.
[83] A. C. Baratunde, X. Xianfan, and S. F. Timothy, "Increased real contact in thermal interfaces: A carbon nanotube/foil material," *Applied Physics Letters,* vol. 90, 2007.
[84] A. C. Baratunde, X. Jun, and S. F. Timothy, "Contact mechanics and thermal conductance of carbon nanotube array interfaces," *International Journal of Heat and Mass Transfer,* vol. 52, 2009.
[85] A. Majumdar and P. Reddy, "Role of electron–phonon coupling in thermal conductance of metal–nonmetal interfaces," *Applied Physics Letters,* 2004.
[86] J. Ordonez-Miranda and J. Alvarado-Gil…, "The effect of the electron-phonon coupling on the effective thermal conductivity of metal-nonmetal multilayers," *Journal of Applied ...,* 2011.
[87] L. S. P. Kim, A. Majumdar, and P.L. McEuen, "Thermal Transport Measurements of Individual Multiwalled Nanotubes," *Physical Review Letters,* vol. 87, 2001.
[88] P. Ravi, "Thermal boundary resistance and thermal conductivity of multiwalled carbon nanotubes," *Physical Review B,* vol. 77, 2008.
[89] G. Chen, "Thermal conductivity and ballistic-phonon transport in the cross-plane direction of superlattices," *Physical Review B,* vol. 57 (23), 1998.
[90] R. Prasher, "Predicting the thermal resistance of nanosized constrictions," *Nano letters,* vol. 5, pp. 2155-2159, 2005.
[91] L. H. D. Siegel, J. Adams, "Adhesion, Atomic Structure, and Bonding at the α–Al2O3(0001)/Al(111) Interface: A First Principles Study," *Physical Review B,* vol. 65, 2000.
[92] T. Ebbesen, H. Lezec, H. Hiura, and J. Bennett…, "Electrical conductivity of individual carbon nanotubes," 1996.
[93] Wikipedia. (2014). *Electrical resistivity and conductivity*. Available: http://en.wikipedia.org/wiki/Electrical_resistivity_and_conductivity
[94] (2000-2014). *Alumina - supplier data by Ceramerat*. Available: http://www.azom.com/article.aspx?ArticleID=3382
[95] M. Park, B. Cola, T. Siegmund, and J. Xu…, "Effects of a carbon nanotube layer on electrical contact resistance between copper substrates," *...,* 2006.

[96] A. Cao, C. Xu, J. Liang, D. Wu, and B. Wei, "X-ray diffraction characterization on the alignment degree of carbon nanotubes," *Chemical physics letters,* 2001.
[97] S. Aruna, V. Grips, and K. Rajam, "Synthesis and characterization of Ni–Al2O3 composite coatings containing different forms of alumina," *Journal of applied electrochemistry,* 2010.
[98] S. Yun, K. Lee, J. Skarp, and H. Kim…, "Dependence of atomic layer-deposited Al2O3 films characteristics on growth temperature and Al precursors of Al (CH3) 3 and AlCl3," *Journal of Vacuum ...,* 1997.
[99] N. Bertrand, C. Desgranges, D. Poquillon, M.-C. Lafont, and D. Monceau, "Iron oxidation at low temperature (260–500 C) in air and the effect of water vapor," *Oxidation of metals,* vol. 73, pp. 139-162, 2010.
[100] J. L. v. Hemmen, S. B. S. Heil, J. H. Klootwijk, F. Roozeboom, C. J. Hodson, M. C. M. v. d. Sanden, *et al.*, "Plasma and Thermal ALD of Al[sub 2]O[sub 3] in a Commercial 200 mm ALD Reactor," *Journal of The Electrochemical Society,* vol. 154, 2007.
[101] A. Cavanagh, C. Wilson, and A. Weimer…, "Atomic layer deposition on gram quantities of multi-walled carbon nanotubes," *...,* 2009.
[102] G. Nessim, A. Hart, J. Kim, D. Acquaviva, and J. Oh…, "Tuning of vertically-aligned carbon nanotube diameter and areal density through catalyst pre-treatment," *Nano ...,* 2008.
[103] J. Taphouse, O. Smith, and S. Marder…, "A pyrenylpropyl phosphonic acid surface modifier for mitigating the thermal resistance of carbon nanotube contacts," *Advanced Functional ...,* 2014.